AB INITIO INVESTIGATION OF THE NANOTRIBOLOGICAL PROPERTIES OF MOS_2/AU(111) INTERFACE

A THESIS SUBMITTED TO
THE GRADUATE SCHOOL OF NATURAL AND APPLIED SCIENCES
OF
MIDDLE EAST TECHNICAL UNIVERSITY

BY

ÜMIT DOĞAN DAĞLUM

IN PARTIAL FULFILLMENT OF THE REQUIREMENTS
FOR
THE DEGREE OF MASTER OF SCIENCE
IN
PHYSICS

JANUARY 2020

Approval of the thesis:

AB INITIO INVESTIGATION OF THE NANOTRIBOLOGICAL PROPERTIES OF $\mathbf{MOS_2}$/AU(111) INTERFACE

submitted by **ÜMIT DOĞAN DAĞLUM** in partial fulfillment of the requirements for the degree of **Master of Science in Physics Department, Middle East Technical University** by,

Prof. Dr. Dr. Halil Kalıpçılar
Dean, Graduate School of **Natural and Applied Sciences** ________________

Prof. Dr. Altuğ Özpineci
Head of Department, **Physics** ________________

Assoc. Prof. Dr. Hande Toffoli
Supervisor, **Physics, METU** ________________

Examining Committee Members:

Assoc. Prof. Dr. Seymur Jahangirov
UNAM, Bilkent University ________________

Assoc. Prof. Dr. Hande Toffoli
Physics, METU ________________

Assoc. Prof. Dr. Alpan Bek
Physics, METU ________________

Date: 16.01.2020

I hereby declare that all information in this document has been obtained and presented in accordance with academic rules and ethical conduct. I also declare that, as required by these rules and conduct, I have fully cited and referenced all material and results that are not original to this work.

Name, Surname: Ümit Doğan Dağlum

Signature :

ABSTRACT

AB INITIO INVESTIGATION OF THE NANOTRIBOLOGICAL PROPERTIES OF MOS$_2$/AU(111) INTERFACE

Dağlum, Ümit Doğan
M.S., Department of Physics
Supervisor: Assoc. Prof. Dr. Hande Toffoli

January 2020, 50 pages

Microscopic system is not obey classic friction concept due to atomic interaction and quantum effect in nano scale such as van der Waals forces etc. Therefore, each system display different friction behavior so they should studied one by one. Nanotribology which is sub-field of tribology studies friction at the two dimensional structure such as graphene, silicen and TMD's material using Density Functional Theory. Moreover, atomic force microscopy (AFM) and friction force microscopy (FFM) are used reveal friction behavior and lubricant behavior of structures to help nanotribological stuides. In this thesis, we studied the nanotribological properties of MoS$_2$/Au(111) interface using Density Functional Theory (DFT). Electronic,atomic orbital and phonon structure of MoS$_2$ is examined. We identify and discuss friction force trends for each different applied vertical load. To reveal the most optimum path to take for AFM tip on MoS$_2$ structure, energy corrugation is calculated for MoS$_2$/Au(111) interface.

Keywords: nanotribology, Density Functional Theory, Computational Physics, MoS$_2$, friction, potential surface energy

ÖZ

MOS2/AU(111) YÜZEYİNİN BAŞLANĞIÇTAN İTİBAREN NANOTRİBOLOJİK ÖZELLİKLERİNİN İNCELENMESİ

Dağlum, Ümit Doğan
Yüksek Lisans, Fizik Bölümü
Tez Yöneticisi: Doç. Dr. Hande Toffoli

Ocak 2020 , 50 sayfa

Atomların etkileşimleri ve kuantum etkileri nedeniyle mikrokopik sistemler klasik sürtünme konseptine uygun hareket etmezler. Bu nedenle, her sistem farklı sürtünme davranışı gösterir yani sistemler teker teker incelenmelidir. Tribolojinin alt alanlarından olan nanotriboloji iki boyutlu sistemlerde yoğunluk fonksiyoneli teorisi (YFT) kullanarak sürtünme çalışır. Ek olarak, Atom Kuvvet Mikroskobu(AKM) ve Sürtünme Kuvveti Mikroskobu(SKM) materyellerin sürtünme ve kayganlık davranışlarını ortaya çıkararak nanotribolojik çalışmalara yardımcı olur.Bu tezde, MoS_2/Au(111) arayüzünün nanotribolojik özellikleri yoğunluk fonksiyoneli teorisi (YFT) kullanılarak çalışdık. MoS_2 yapısının elektriksel, atomik orbital ve fonon yapısını inceledik. Sürtünme kuvvetinin yönelimini her bir dik uygulamış yük ile tanımladık ve tartıştık. Atom Kuvvet Mikroskobunun (AKM) uçunun katetmesi gereken en ideal yolu ortaya çıkarmak için potensiyel enerji yüzeyini hesapladık.

Anahtar Kelimeler: nanotriboloji, Yük Yoğunluğu Fonksiyoneli Teorisi, Hesaplamalı Fizik, MoS_2, sürtünme, potansiyel enerji yüzeyi

To my mother

ACKNOWLEDGMENTS

First, I would like to thank my advisor Assoc. Prof. Dr. Hande Toffoli for being a good mentor and helpful teacher for me. I also want to thank Assoc. Prof. Dr. Seymur Jahangirov for his guidance and support during the first semester of my master's.

I am grateful to have a very supportive and joyful family. They always make me feel safe even when my mind state is chaotic. Especially my mother Hatice Erkan help me to find a way to avoid the darkest thoughts even if it is hard for her.

I am also lucky to have friends share the same intellectual taste with me during university life and also all of them gave me a hand when I had a difficult situation. Even if they are far away, they will always going to be by my side with the warmth of memories. I also want to thank office 334 members especially Fırat. Also, I want to thank Cihan who advise me in rough situations. Moreover, I want to thank my friends who are always be a member of my power rangers team: Ahmet, Beyza, Merve, Onur, Özgür, and Seçil. The biggest thanks go to my best friend and my travel companion Büşra Erdoğan. She has always been the light in my darkest moments.

This work is financially supported by TÜBITAK (The Science and Technological Research Council of Turkey).(Grant no:115F493)

TABLE OF CONTENTS

ABSTRACT v

ÖZ vi

ACKNOWLEDGMENTS viii

TABLE OF CONTENTS ix

LIST OF TABLES xi

LIST OF FIGURES xii

LIST OF ABBREVIATIONS xv

CHAPTERS

1 INTRODUCTION 1

2 THEORETICAL METHODS 9

  2.1 Density Functional Theory 9

  2.2 Electron Density 10

  2.3 Hohenberg-Kohn Theorems 11

  2.4 Kohn-Sham Equation 15

  2.5 Local Density Approximation 18

  2.6 Generalized Gradient Approximation 19

  2.7 Hybrid functionals 19

  2.8 The van-der Waals Interaction 20

3 RESULT AND DISCUSSION 23

3.1 Preliminary Calculations 24

3.1.1 Molybdenum disulfide 24

3.1.2 Hybrid Functional of MoS_2's band structure 25

3.1.3 Au Bulk Structure 26

3.2 The MoS_2/Au(111) 27

3.2.1 Finding an appropriate simulation cell 27

3.2.2 Load Dependence of Energy and Friction Force 30

4 CONCLUSION 43

REFERENCES 47

LIST OF TABLES

TABLES

Table 1.1 Electrical Resistance of a Circular Constriction in a Copper–Copper Interface 6

Table 3.1 Percentage strain for adjustment of Au(111) and MoS_2 surface unit cell 28

LIST OF FIGURES

FIGURES

Figure 1.1 Coulomb's model for friction. (a) An object is at equilibrium at a given point on rough surface held in place by a lateral force and static friction. (b) Free-body diagram of the object. 2

Figure 1.2 The Prandtl model: A point mass dragged in a periodic potential. 3

Figure 1.3 Characteristic of motion for slip-stick effect in friction. 4

Figure 1.4 Representational AFM illustration. [15] 7

Figure 2.1 Schematic representation of the HK mapping 12

Figure 3.1 (a) MoS_2 structure.(b)Energy versus lattice constants for MoS_2 structure 24

Figure 3.2 (a) Band structure of monolayer MoS_2.(b) DOS of MoS_2 single layer 25

Figure 3.3 Phonon dispersion curves of MoS_2 layer. 25

Figure 3.4 (a) Band structure of monolayer MoS_2 with HSE06($\alpha = 0.25$).(b) Band structure of monolayer MoS_2 with HSE06($\alpha = 0.1$) 26

Figure 3.5 Total energy vs lattice constant of bulk Au. 27

Figure 3.6 (a)MoS_2 and Au(111) unit cell configuration on side view and (b)MoS_2 and Au(111) unit cell configuration on side view 28

Figure 3.7 The configuration of top layer of Au(111) and MoS_2 layer 28

Figure 3.8 Equilibrium separation distance and interaction energy between MoS_2 layer and Au(111) surface 29

Figure 3.9 (a)Top side of interface and (b)side view of interface. The red and blue isosurfaces represent to positive and negative charge difference with isosuface 0.0006 30

Figure 3.10 (a)Average charge density of the interface which has vdW energy along z axis (b)Average charge density of the interface which has no vdW energy along z axis 30

Figure 3.11 Lateral displacement sites of MoS_2/Au(111) interface (a)displacement 0 Å in x-axis. (b)displacement 0.4 Å in x-axis. (c) displacement 0 Å in y-axis. (d) displacement 0.6 Å in y-axis 31

Figure 3.12 lateral friction force of vertically loaded Au(111)-MoS_2 structure in several orders in x direction.(a) 0 eV Load.(b) 2 eV Load.(c) 8 eV Load. (d)10 ev Load. (e) 12 eV Load. (f) 14 eV Load 32

Figure 3.13 Lateral friction force of vertically loaded Au(111)-MoS_2 structure in several orders in y direction .(a) 0 eV/Å Load.(b) 2 eV/Å Load.(c) 8 eV/Å Load. (d)10 eV/Å Load. (e) 12 eV/Å Load. (f) 14 eV/Å Load . 33

Figure 3.14 Position of MoS_2 structure in x axis versus z axis .(a) 0 eV/Å Load.(b) 2 eV/Å Load.(c) 8 eV/Å Load. (d)10 eV/Å Load. (e) 12 eV/Å Load. (f) 14 eV/Å Load 34

Figure 3.15 (a) Average lateral friction force (b)friction coefficient with increasing applied load over MoS_2-Au(111) interface configuration in x direction sliding path 35

Figure 3.16 (a) Average lateral friction force (b)friction coefficient with increasing applied load over MoS_2-Au(111) interface configuration in y direction sliding path 36

Figure 3.17 Isosurfaces and variation of linear density of charge density difference along z-axis.(a) 4 eV/Å Load.(b) 10 eV/Å Load.(c) 12 eV/Å Load. (d)14 eV/Å Load. 37

Figure 3.18 (a)The potential surface calculation graph of $Au(111)/MoS_2$ with labels.(b) Label A configuration.(c) Label B configuration. (d)Label C configuration. 38

Figure 3.19 (a)The potential surface calculation graph with minimum energy path.(b) Energy versus displacement.(c) Force versus displacement. . . 39

Figure 3.20 Isosurfaces and variation of linear density of charge density difference long z-axis on max point of PES. Blue isosurfaces plots correspond to the charge density depletion, yellow one correspond to accumulation and isosuface is 0.0006 40

Figure 3.21 Isosurfaces and variation of linear density of charge density difference long z-axis on saddle point (a,b) and on minimum point (c,d) of PES. 42

LIST OF ABBREVIATIONS

ABBREVIATONS	
2D	2 Dimensional
AFM	Atomic Force Microscopy
FFM	Friction Force Microscopy
STM	Scanning Tunneling Microscope
PT Model	Prandtl Tomlinson Model
DFT	Density Functional Theory
KS	Kohn-Sham
LDA	Local Density Approximation
GGA	Generalized Gradient Approximation
vdW	van der Waals
HSE	Heyd-Scuserin-Ernzerholf
PBE	Perdew-Burke-Ernzerhof exchange functional
SCF	Self Consistent Field
VASP	Vienna Ab initio Simulation Package
PES	Potential Energy Surface

CHAPTER 1

INTRODUCTION

The friction phenomena have been studied and humankind tried to find ways to reduce it, since humans began to carry material on rough surface for building antic structure. In the light of friction phenomena, humankind have built modern machineries where brackets in car engines, driving wheels and railways etc. On the other hand, friction force cause loss of energy in this industrial systems and the loss of energy should prevented (at least reduced) for future of our ecosystem. To overcome this situation, friction phenomena should be understood on atomic scale however because of technological inadequacies, scientists can only study friction force on macro scale.

Beginning of friction study on macro scale can be traced as far back as 1493. The first fundamental laws of friction was noted by Leonardo da Vinci. According to da Vinci, friction laws can be summarized in two statements :

1) Contact area has have no effect on friction.

2) If the load of an object is doubled, its friction will also be doubled [1].

These laws never have been published by Leonardo da Vinci. After 200 years, Guillaume Amontons rediscovered da Vinci's friction laws and these laws came to be known as Amontons' three laws of dry friction. He explained the nature of friction in terms of surface irregularities. All of these laws can be summed up in three statement [2] :

1) The force of friction is directly proportional to the applied load. (Amontons' 1st

law)

2) The force of friction is independent of the apparent area of contact. (Amontons' 2nd law)

3) Kinetic friction is independent of the sliding velocity. (Coulomb's law)

These statements were formulated in a single equation by Sir Isaac Newton :

$$F = \mu F_N \tag{1.1}$$

where F is the friction force, μ is a friction coefficient which is the ratio of the force of friction between two bodies and the force pressing them together and F$_N$ is a normal force which applied by each surface on the other. Beyond these fundamental statements, Charles-Augustin de Coulomb proposed the first model of the physical origin of friction. According to Coulomb, the interaction between micro-roughnesses of both contacting surfaces is responsible for the force of friction. The model of Coulomb's theory is represent in Fig.1.1

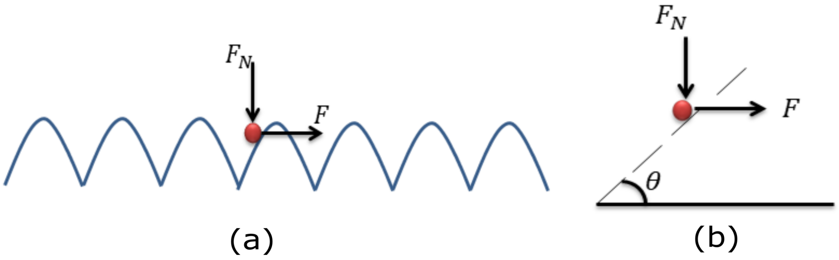

Figure 1.1: Coulomb's model for friction. (a) An object is at equilibrium at a given point on rough surface held in place by a lateral force and static friction. (b) Free-body diagram of the object.

From free-body diagram ,friction's formulation is derived :

$$F = mgsin(\theta) \tag{1.2}$$

$$F_N = mgcos(\theta) \tag{1.3}$$

From Eq.1.2 and Eq.1.3,

$$F = F_N tan(\theta) \tag{1.4}$$

The static friction force F_s is equal to maximum value of F, by definition. The Eq.1.4 is still hold for this case :

$$F_s = F_{max} = F_N tan(\theta_{max}) \tag{1.5}$$

Therefore, the coefficient of static friction is equal to the maximum slope of the surface:

$$\mu_s = \frac{F_s}{F_N} = tan(\theta_{max}) \tag{1.6}$$

Coulomb's model simply provides a link of the coefficient of friction geometry.

The Prandtl-Tomlinson(PT) model was proposed in 1928 and describes a plastic deformation in the crystal. This model provides an explanation on the effect velocity, elastic constant and the plasticity on friction. Therefore, PT model is widely used in the investigation of frictional mechanisms in nanotribology. This model is basically built with many elastically coupled "atoms" moved along a periodic potential. The periodic potential is represented as a spring and the atom is moved on a one dimensional surface with constant velocity v_0 as shown as Fig1.2. The damping term is proportional to velocity.

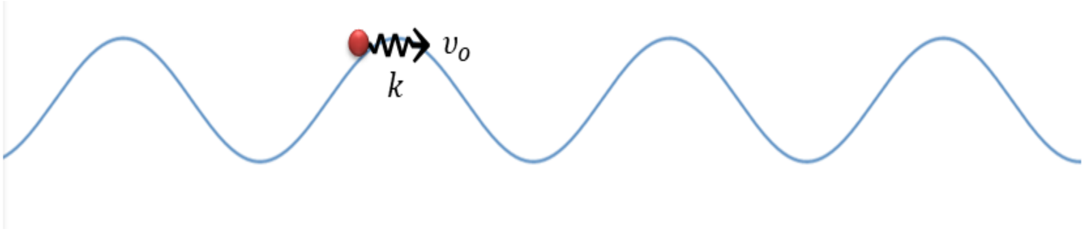

Figure 1.2: The Prandtl model: A point mass dragged in a periodic potential.

This motion can be formulated as follows :

$$m\ddot{x} = k(v_0 t - x) - N sin(2\pi/a) - \eta\dot{x} \tag{1.7}$$

where k is the stiffness of the spring, m is the mass of atom(body), x is the coordinate of the atom(body), a the spatial period of the potential η is the damping coefficient and N the amplitude of the periodic force.

The PT model probes two different aspect of the friction concept :

1)Without a damping effect on velocity, sliding forces can not exist in the macroscopic sense.

2)Without a conservative force, static friction can not exist.

In light of these result, stick-slip effect in friction can be examined [3] . The relation between the stiffness of spring and potential barrier demonstrate stick-slip behavior. When the elastic energy of the body is large enough to overcome the potential barrier, it exhibits continuous movement along the direction of motion. On the other hand, if the material stiffness is bigger than spring stiffness $k_c > k_s$, stick-slip effect is observed. The system suddenly jumps between local minima as Fig 1.3.

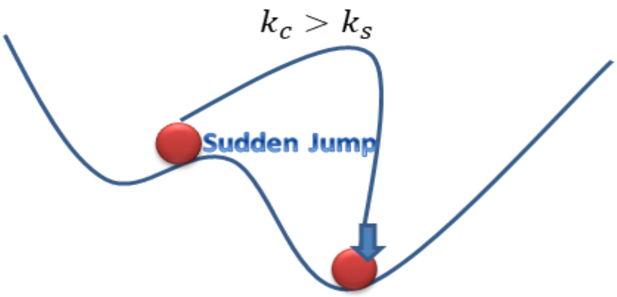

Figure 1.3: Characteristic of motion for slip-stick effect in friction.

The conventional version of friction theorems state that friction force is proportional to load and is independent of the size of contact area. This statement holds for macroscopic materials and experimental works proved that. However, at the atomic scale, friction force cannot be examined via arguments based on a macroscopic contact area. In 1950, Bowden and Tobar [4] published a theorem which include two important statements for friction force at the atomic scale:

1) Macroscopic contact area cannot be analyze without micro-contacts due to molecular properties exerts forces such as Adhesion force and elastic deformation on micro-contacts include sheer stress in a complicated dynamic process.

2)The deformation force which occurs arises from the ploughing, grooving or cracking of one surface by asperities on the other. The formulation of these process is :

$$F = F_{adhesion} + F_{deformation} = sA + P \tag{1.8}$$

where A is the real contact area, s is a sheer stress of the junction and P is the deformation term. The main quest for examining this theorem is to detect the real contact area. Bowden and Tobar also developed a method which is used for detecting real contact area [5]. This method measure real contact area using electrical conductivity. For simplicity, contact area is assumed to be circular and continuous. The shape of contact with a radius a is contracted by electrical contraction with using equipotential surfaces of flow. The equipotential lines are represented by ellipsoid coordinate equation.

$$\frac{r^2}{\mu^2 + a^2} + \frac{z^2}{\mu^2} = 1 \tag{1.9}$$

where μ is the length of the vertical semi-axis of the ellipsoid and r,z are cylindrical coordinate.The resistance between the equipotential surface with semi-axis μ and the constriction is given as

$$R_\mu = \frac{\rho}{2\pi} \int_0^\mu \frac{d\mu}{\mu^2 + a^2} = \frac{\rho}{2\pi a} arctan(\frac{\mu}{a}) \tag{1.10}$$

where ρ is the resistivity of the conductor. When ρ is very large, the construction resistance between equipotential surface and constriction Eq. 1.10 became the spreading resistance

$$\lim_{\mu \to \infty} R_\mu = R_s = \lim_{\mu \to \infty} \frac{\rho}{2\pi} \int_0^\mu \frac{d\mu}{\mu^2 + a^2} = \lim_{\mu \to \infty} \frac{\rho}{2\pi a} arctan(\frac{\mu}{a}) \tag{1.11}$$

and $\lim_{\mu \to \infty} arctan(\frac{\mu}{a}) = \frac{\pi}{2}$ Eq. 1.11 equal to

$$R_s = \frac{\rho}{4a}. \tag{1.12}$$

The total contraction resistant for contact area is twice as spreading resistance R_s

$$R_c = \frac{\rho}{2a}. \tag{1.13}$$

Eq. 1.12 and Eq. 1.13 is give us change to detect real contact area with using electrical constriction. The relation between them see in table 1.1 [6]

The construction of friction theories and detecting the real contact area allow to the experimental measurement of friction coefficients. The most popular measuring tool

Table 1.1: Electrical Resistance of a Circular Constriction in a Copper–Copper Interface

a radius(μm)	Constriction Resistance(Ω)
0.01	0.88
0.1	8.8×10^{-2}
1	8.8×10^{-3}
10	8.8×10^{-4}

is Atomic Force Microscope(AFM) which is a probe-based microscope on a flexible cantilever and produces very high resolution 3-D images of the surface as shown figure 1.4 . The AFM can perform measurements for both electrical insulation and conducting materials and is able to measure ultra-small forces between $1\mu m$ and $1nm$. There are three operation modes in AFM [7], contact mode, non-contact mode and tapping. In contact mode, the probe is in contact with the sample surface. During operation, The Van der Waals forces create a repulsive effect due to electronic orbital overlap with the atoms in the sample surface. The force on the probe causes the cantilever deflection and this deflection is measured by capacitive,tunnelling or optical detectors. Finally, the image of the sample surface is obtained from measurement data. In tapping mode, the cantilever vibrates with a sinusoidal frequency over the sample surface during the scanning process. This method is mostly used in biological samples. Finally in non-contact mode, the probe is not in contact with the sample surface it can only be operated at very close distance for example $0.1 - 10nm$ probe-surface separation. The cantilever is deliberately vibrated either in frequency modulation (FM) mode or amplitude modulation (AM) mode and during the scanning process the Van der Waals forces create attractive force between the probe and the sample surface. Moreover, with a modification, AFM can be measure the normal forces and the lateral forces. This microscopy know as Friction Force Microscope or Lateral Force Microscope [8] [9] [10] [11] [12] [13] [14]. In the light of these models and experimental development, humanity is able to enlighten friction phenomena at the atomic scale .

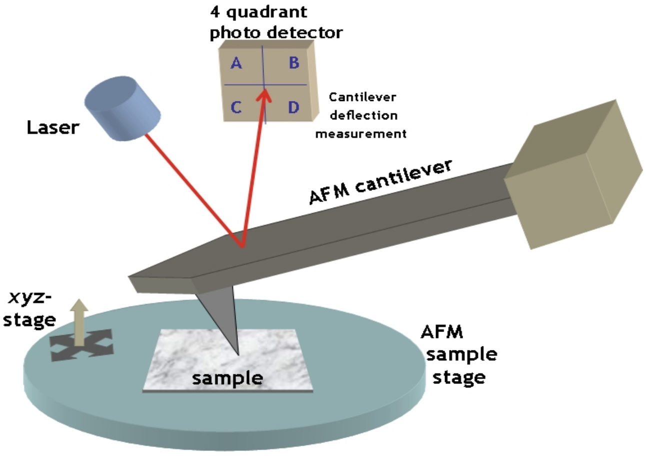

Figure 1.4: Representational AFM illustration. [15]

Two dimensional layered materials have remarkable performance as solid lubricants due to their physical, mechanical and chemical properties. Therefore 2D materials gained importance in scientific community in recent years. In 2012, Cahangirov [16] and his team conducted a theoretical on honeycomb 2D structure such as MoS_2, WO_2,graphane and fluorographene for determining the frictional figures of merit using the Prandtl-Tomlinson model.They derived the critical stiffness required to avoid stick-slip behavior and concluded that two sliding layered nanostructures perform continuous sliding with ultralow friction. These nanostructures were therefore identified as superlubric materials. In the another study of Cahangirov and his team in 2018, they calculated phonon modes and finite temperature molecular dynamics of low-buckled, honeycomb structures such as germanium and silicon and they are concluded electronic and magnetic properties of germanium and silicon depends on their size and geometry [17] . This paper proved to understand MoS_2 electronic properties. In another study of Cahangirov and his team a single layer graphene was placed between two parallel Ni(111) interfaces to screen the interaction that cause adhesion and sliding process. This study proved, strong interaction between the Ni(111) sliding surface reduces significantly by one layer graphene when it is placed between the Ni(111) surfaces [18] .

The MoS_2/graphene interface has superlubricity properties. The study conducted by Wang et.al [19] found that the sliding induced charge density fluctuations which are a key to understand potential surface energy and atomic scale friction. The superlubric behavior of MoS_2 is conducted by Li et al. [20] . They developed a method for studying the friction properties between atomic layered materials. This method combined the in situ scanning electron microscope technique with a silicon nanowire force sensor to detected ultra low friction coefficient of MoS_2. They found friction coefficient of MoS_2 is 10^{-4} in regime of superlubricity.

In this thesis, electronic,chemical and phonon properties of MoS_2 has been studied. After that, MoS_2/Au(111) interfaces have been modeled and investigated using first-principle calculations to examined the nanotribological properties of the interface using Density Functional Theory(DFT). MoS_2/Au(111) interface is a model for friction force microscopy(FFM) and atomic force microscopy(AFM) experiments since it is expected to reveal superlubric behaviour. We studied and identified behaviour of friction trend with different vertical load for experimentally feasible contact area.

CHAPTER 2

THEORETICAL METHODS

2.1 Density Functional Theory

One of the basic problems in chemistry and physics is the determination of structure and dynamics of many-electron systems.However, closed form solutions of the Schrodinger equation are inaccessible due to the electron correlations for even the smallest systems. For a multiatomic system, the many-particle Schrödinger equation is

$$H\Psi(\vec{\mathbf{R}}_1, ..., \vec{\mathbf{R}}_N, \vec{\mathbf{r}}_1, ..., \vec{\mathbf{r}}_n) = E\Psi(\vec{\mathbf{R}}_1, ..., \vec{\mathbf{R}}_N, \vec{\mathbf{r}}_1, ..., \vec{\mathbf{r}}_n) \tag{2.1}$$

Where $\vec{\mathbf{R}}_i$ and $\vec{\mathbf{r}}_i$ are the nuclear and the electronic positions.
The solution of equation Eq. 2.1 can be complicated due to the large number of variables. Recognizing the fact that the nuclei are several thousands of times heavier than electrons, the many particle system is divided into two : electronic and nuclear degree of freedom. This process is known as the Born-Oppenheimer approximation [21].

$$\Psi(\vec{\mathbf{R}}_1, ..., \vec{\mathbf{R}}_N, \vec{\mathbf{r}}_1, ..., \vec{\mathbf{r}}_n) = \Psi^n(\vec{\mathbf{R}}_1, ..., \vec{\mathbf{R}}_N)\Psi^e(\vec{\mathbf{r}}_1, ..., \vec{\mathbf{r}}_n) \tag{2.2}$$

where Ψ^n is nuclear wave-function and Ψ^e is electron wave-function which depends parametrically on the position of the nuclei. After the Born-Oppenheimer approximation, Schrödinger Eq. 2.1 becomes

$$H\Psi^e(\vec{\mathbf{R}}_1, ..., \vec{\mathbf{R}}_N, \vec{\mathbf{r}}_1, ..., \vec{\mathbf{r}}_n) = E(\vec{\mathbf{R}}_1, ..., \vec{\mathbf{R}}_N)\Psi^e(\vec{\mathbf{R}}_1, ..., \vec{\mathbf{R}}_N, \vec{\mathbf{r}}_1, ..., \vec{\mathbf{r}}_n) \tag{2.3}$$

where $E(\vec{\mathbf{R}}_1, ..., \vec{\mathbf{R}}_N)$is ground state energy of nuclei and it is known as the adiabatic potential energy surface of the atoms.
The approximate solution of this equation can be achieved either by employing wavefunction or based methods. The simplest approximation to the wavefunction can be constructed by means of a single Slater determinant and optimizing it within the variational approach. This method is referred to as the Hartree-Fock approximation [22] [23] . However, Hartree-Fock Method is limited to small systems and excludes correlation effects. Therefore, a better-suited theory(or approach) has to go beyond the Hartee-Fock method. One idea would be to translate the N-particle system to an effective single electron problem including the correlation.Such an approach, namely the density functional theory (DFT) was developed in 1965 [24]. In this chapter, we cover the fundamentals of DFT.

2.2 Electron Density

The solution of Eq.2.3 is a difficult task to achieve for every system due to the complexity of wave-functions in 3N dimensions. To overcome this difficulty, density functional theory provides an alternative. The key ingredient is the electron density represented by the operator,

$$\hat{n}(\vec{\mathbf{r}}) = \sum_{i=1}^{N} \delta(\vec{\mathbf{r}} - \vec{\mathbf{r}}_i). \tag{2.4}$$

Where $\delta(\vec{\mathbf{r}} - \vec{\mathbf{r}}_i)$ is contribution to the density operator of i^{th} electron, $\vec{\mathbf{r}}_i'$ is the position of the i^{th} electron and N is the total number of electrons. Eq. 2.4 is related to the probability of finding an electron at point $\vec{\mathbf{r}}$ 3-D space. The density obtained by substituting density operator in 2.4 into the many-body wave-function

$$
\begin{aligned}
& n(\vec{\mathbf{r}}) = \langle\Psi|\,\hat{n}(r)\,|\Psi\rangle \\
& = \int \Psi^*(\vec{\mathbf{r_1}},\vec{\mathbf{r_2}},...,\vec{\mathbf{r_N}}) \sum_{i=1}^{N} \delta(\vec{\mathbf{r}}-\vec{\mathbf{r}}'_i)\Psi(\vec{\mathbf{r_1}},\vec{\mathbf{r_2}},...,\vec{\mathbf{r_N}})d\vec{\mathbf{r_1}}d\vec{\mathbf{r_2}}...d\vec{\mathbf{r_N}} \\
& = \int \Psi^*(\vec{\mathbf{r_1}},\vec{\mathbf{r_2}},...,\vec{\mathbf{r_N}})\Psi(\vec{\mathbf{r}},\vec{\mathbf{r_2}},...,\vec{\mathbf{r_N}})d\vec{\mathbf{r_2}}...d\vec{\mathbf{r_N}} \\
& + \int \Psi^*(\vec{\mathbf{r_1}},\vec{\mathbf{r}},...,\vec{\mathbf{r_N}})\Psi(\vec{\mathbf{r_1}},\vec{\mathbf{r_2}},...,\vec{\mathbf{r_N}})d\vec{\mathbf{r_1}}d\vec{\mathbf{r_3}}...d\vec{\mathbf{r_N}} \\
& + ... \\
& = N \int \Psi^*(\vec{\mathbf{r}},\vec{\mathbf{r_2}},...,\vec{\mathbf{r_N}})\Psi(\vec{\mathbf{r_1}},\vec{\mathbf{r_2}},...,\vec{\mathbf{r_N}})d\vec{\mathbf{r_2}}d\vec{\mathbf{r_3}}...d\vec{\mathbf{r_N}} \\
& = N \int |\Psi(\vec{\mathbf{r}},\vec{\mathbf{r_2}},...,\vec{\mathbf{r_N}})|^2 d\vec{\mathbf{r_2}}d\vec{\mathbf{r_3}}...d\vec{\mathbf{r_N}} \\
& = n(\vec{\mathbf{r}}).
\end{aligned}
\tag{2.5}
$$

The integration of density all over the whole space should give the total number of electrons

$$\int n(\vec{\mathbf{r}})d\vec{\mathbf{r}} = N. \tag{2.6}$$

Next we prepare the framework for the expression of the total energy in terms of the density rather than the wavefunction.

2.3 Hohenberg-Kohn Theorems

Hohenberg-Kohn theorems(HK) is a starting point for any discussion of DFT. They represent the most basic of a number of existence theorems which the ensure that stationary many-particle systems can be characterized by the ground state density and closely related quantities [25] .The mathematical steps of HK begin withthe following expression of the time-indepndent Hamiltonian of the many-particle system is:

$$\hat{H} = \hat{T} + \hat{V}_{ext} + \hat{W} \tag{2.7}$$

Where $\hat{T}$ is kinetic energy operator,$\hat{W}$ is the particle interaction energy operator and $\hat{V}_{ext}$ is single particle potential energy operator.

$$\hat{T} = \sum_{j=1}^{N} \frac{(-i\hbar\nabla_j)^2}{2m} \tag{2.8}$$

$$\hat{W} = \sum_{i,j=1;i<j}^{N} w(r_i, r_j) = \frac{1}{2} \sum_{i,j=1;i\neq j}^{N} w(\vec{\mathbf{r}}_i, \vec{\mathbf{r}}_j) \tag{2.9}$$

$$\hat{V} = \sum_{j=1}^{N} \nu_{ext}(\vec{\mathbf{r}}_i) = \int d^3r \nu_{ext}(\vec{\mathbf{r}}_i) n(\vec{\mathbf{r}}) \tag{2.10}$$

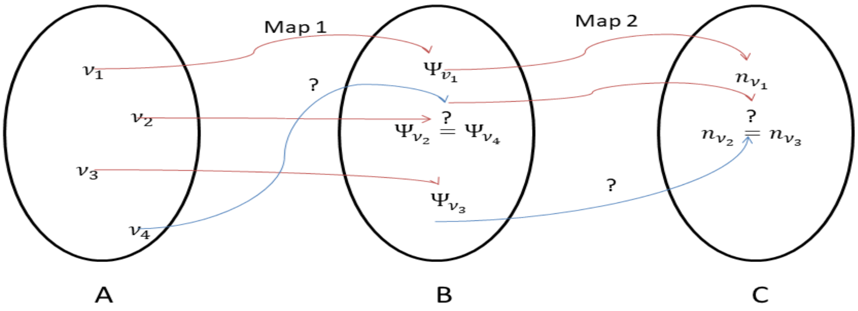

Figure 2.1: Schematic representation of the HK mapping

The solution of the Schrödinger equation with set of all Hamiltonian of form Eq. 2.4 can be interpreted as a map between external potentials, ground states and ground state densities(See Fig:2.1). In order to find out the solution we should answer two questions regarding the maps :

1)Do two external potential can map one ground state ?

2)Do one ground state can map two ground states density ?

These questions are answered by HK: Maps are injective and therefore unique which are demonstrating two statement :

1) for given ν_{ext} there is only one $|\Psi_o\rangle$ exist in B. This means no two v_{ext} mapped onto one $|\Psi_o\rangle$ in B.

Proof :

Assume two different external potentials V^1_{ext} and V^2_{ext} which belong to distinct Hamiltonians $\hat{H}^1_{ext}$ and $\hat{H}^2_{ext}$ which operate same wave-function $|\Psi_o\rangle$.

$$\hat{H}^1 |\Psi_o\rangle = \hat{T} + \hat{W} + \hat{V}^1_{ext} |\Psi_o\rangle = E^1_o |\Psi_o\rangle \tag{2.11}$$

$$\hat{H}^2 |\Psi_o\rangle = \hat{T} + \hat{W} + \hat{V_{ext}^2} |\Psi_o\rangle = E_o^1 |\Psi_o\rangle \tag{2.12}$$

Subtracting Eq.2.11 from Eq.2.12

$$\hat{V_{ext}^1} |\Psi_o\rangle - \hat{V_{ext}^2} |\Psi_o\rangle = E_o^1 - E_o^2 |\Psi_o\rangle \tag{2.13}$$

When the information change in ground state wave-function for example position of nuclei, LHS of equation 2.13 change however RHS of equation 2.13 remain same. This situation create a conflict. As a result, external potential determines uniquely the ground state wave-function

2) Two different ground state can not map to one ground state density.
Proof :

Assume two different ground state $|\Psi_o\rangle$,$|\Psi_o'\rangle$ mapped onto ground state density n_o and inequality relation from Ritz variation.

$$E_o = \langle\Psi_o| \hat{H} |\Psi_o\rangle < \langle\Psi_o'| \hat{H} |\Psi_o'\rangle \tag{2.14}$$

Where $\hat{H}$ is unique Hamiltonian leading to $|\Psi_o\rangle$ because of the uniqueness of the Map 1. When the Hamiltonian is operated on ground states.

$$\hat{H} |\Psi_o\rangle = \hat{T} + \hat{V}_{ext} + \hat{W} |\Psi_o\rangle = E_o |\Psi_o\rangle \tag{2.15}$$

$$\hat{H} |\Psi_o\rangle = \hat{T} + \hat{V'}_{ext} + \hat{W} |\Psi_o\rangle = E_o' |\Psi_o\rangle \tag{2.16}$$

The Eq. 2.14 can be express with using Eq. 2.15 and Eq. 2.16

$$E_o < E_o' + W' - W + \langle\Psi_o'| V_{ext}' - V_{ext} |\Psi_o'\rangle \tag{2.17}$$

At this point we may not specify the interaction energy W and W'. Because the form of w is independent in basic DFT formalism.
Insert Eq. 2.10 integral form to 2.17.Then,

$$E_o < E_o' + \int d^3 r n_o(\vec{\mathbf{r}})[\nu_{ext}' - \nu_{ext}] \tag{2.18}$$

we do not know relation between external potential operator, so Eq. 2.17 also can be express as :

$$E'_o < E_o + \int d^3 r n_o(\vec{\mathbf{r}})[\nu_{ext} - \nu'_{ext}] \tag{2.19}$$

The summation of Eq. 2.18 and Eq. 2.19 will be faced with contradiction:

$$E_o + E'_o < E'_o + E_o \tag{2.20}$$

Therefore, This contradiction is leading that the Map 2 is unique : there is a one-to-one correspondence between Ψ_o and n_0.

In the lights of these arguments one can formulate the HK theorem as follows:

1)The Map 1 and Map 2 has one to one correspondence between external potential in Hamiltonian, the solution of the Schrödinger equation is non-degenerate ground state with ground state density and expression is that

$$\nu_{ext}(\vec{\mathbf{r}}) \Longleftrightarrow |\Psi_o\rangle \Longleftrightarrow n_o(\vec{\mathbf{r}}) = \langle\Psi_o|\, \hat{n}_o(\vec{\mathbf{r}})\, |\Psi_o\rangle \tag{2.21}$$

Therefore, $|\Psi_o\rangle$, n_o and ν_{ext} define each others uniquely and mathematical formalism is that $|\Psi[n]\rangle$ which represent ground state is a functional of the ground state density uniquely. This functional define from particular ground state density which $n_o \epsilon$ C with functional of the state.

$$|\Psi_o\rangle = |\Psi[n_o]\rangle \tag{2.22}$$

Eq. 2.21 show that $|\Psi_o\rangle$ is from n_o without explicit information on ν_{ext} and this sitiuation lead that many particle system with same interaction has same functional form of $|\Psi[n]\rangle$ which is universal.

2)Any ground state observable is a density functional due to existence of $|\Psi[n]\rangle$

$$O[n] = \langle\Psi[n]|\, \hat{O}\, |\Psi[n]\rangle \tag{2.23}$$

Eq. 2.23 leads to key expression for DFT.

$$E[n] = \langle\Psi[n]|\, \hat{H}\, |\Psi[n]\rangle = F[n] + \int d^3 r \nu_{ext} n(r) \tag{2.24}$$

$$F[n] = \langle\Psi[n]|\, \hat{T} + \hat{W}\, |\Psi[n]\rangle \tag{2.25}$$

Where $F[n]$ is universal part of ground state observable.

3)There exists a minimum principle for total energy functional $E[n]$:one has for all densities $n'_o(r) \neq n_o(r)$

$$E[n_o] < E[n'_o] \Longleftrightarrow E_o = \min_{n \in C}\{E[n]\} \tag{2.26}$$

The Ritz variational and the unique relation between n_o and Ψ_o show that ground state density($n \in C$) which obtained by solution of Schrödinger equation lead that $\min\limits_{n \in C}\{E[n]\}$.

What is the physical meaning of these three statements?

When there is a change on ν_{ext},their energy is minimized due to to particle reaction, then it's reply is unique. The electron wave-function and density distribution does not need a readjustment. Because there is no modification of external potential due to their locality of potential. For example, when atoms are taken apart, the wave-function and density react with positional change and this change effect external potential. This basic outcome of Hohenberg-Kohn theorem is thus intuitively plausible. In the concussion, HK theorem produce a justification of density functional model that ground state energy represent in terms of ground state density.

$$E_o = E[n_o] \tag{2.27}$$

2.4 Kohn-Sham Equation

Although powerful, Hohenborg-Kohn theorems do not give any explicit from of energy functional $E[n]$ and $F[n]$. The solution of this problem is provided by Kohn-Sham(KS) equation. Before the introduction of KS equation, theoretical tool should be produced for non-interacting system with multiplicative external potential ν_s.

$$\hat{H}_s = \hat{T}_s + \hat{V}_s \quad and \quad \hat{V}_s = \int d^3r \hat{n}(\vec{\mathbf{r}}) \nu_s(\vec{\mathbf{r}}) \tag{2.28}$$

The solution of stationary Schrödinger equation is obtained by Eq. 2.28 with ground state.

$$\hat{H}_s \left|\Psi_o\right\rangle = E_{s,o} \left|\Psi_o\right\rangle \tag{2.29}$$

Schrödinger equation's solution become

$$\{\frac{(-i\hbar\nabla)^2}{2m} + \nu_s(\vec{\mathbf{r}})\}\phi_i(\vec{\mathbf{r}}) = \epsilon_i \phi_i(\vec{\mathbf{r}}) \tag{2.30}$$

The eigenvalues of Eq. 2.30 are ordered as

$$\epsilon_1 \leq \epsilon_2 \leq ...... \leq \epsilon_N = \epsilon_F \leq \epsilon_{N+1} \leq ... \tag{2.31}$$

Where ϵ_F is defined as Fermi energy level which is highest occupied single-particle level.

The general from of ground state density expression when Slater determinat was used

$$n_o(\vec{\mathbf{r}}) = \sum_i^N \int \phi_i^*(\vec{\mathbf{r}})\phi_i^*(\vec{\mathbf{r}})d^3(\vec{\mathbf{r}}). \tag{2.32}$$

Thanks to the HK theorems, the energy can now be written as a functional of density as

$$E[n] = T_s[n] + E_H[n] + E_{ext}[n] + E_{xc}[n]. \tag{2.33}$$

Where $T_s[n]$ is kinetic energy functional of the system and it is found from Eq.2.30

$$T_s[n] = \sum_i^N \int d^3(\vec{\mathbf{r}})\phi_i^*(\vec{\mathbf{r}})\frac{(-i\hbar\nabla)^2}{2m}\phi_i(\vec{\mathbf{r}}). \tag{2.34}$$

$E_H[n]$ is the functional Hartee energy which is interaction energy between the N-particles which have density n.

$$E_H[n] = \int\int d^3(\vec{\mathbf{r}})d^3(\vec{\mathbf{r}}')\frac{n(\vec{\mathbf{r}})n(\vec{\mathbf{r}}')}{|r-r'|}. \tag{2.35}$$

$E_{ext}[n]$ is external energy functional which characterized coupling relation between the particles and external potential

$$E_{ext}[n] = \int d^3(r)\nu_{ext}(\vec{\mathbf{r}})n(\vec{\mathbf{r}}). \tag{2.36}$$

The last term in Eq.2.33 is exchange-correlation energy functional $E_{xc}[n]$ which includes corrections due to electron-electron interaction. Before the examination of the exchange-correlation energy functional, we insert the Kohn-Sham ansatz for the density into single-particle energy expression

$$E_s[n] = \sum_i^N \int d^3(r)\phi_i^*(\vec{\mathbf{r}})\frac{(-i\hbar\nabla)^2}{2m}\phi_i(\vec{\mathbf{r}}) + \frac{1}{2}\int d^3(\vec{\mathbf{r}})d^3(\vec{\mathbf{r}}')\frac{n(\vec{\mathbf{r}})n(\vec{\mathbf{r}}')}{|r-r'|} + \int d^3(\vec{\mathbf{r}})\nu_{ext}(\vec{\mathbf{r}})n(\vec{\mathbf{r}}) + E_{xc}[n]. \tag{2.37}$$

Total energy functional is minimized by ground-state density and it know as "HK variational principle"

$$\frac{\delta E_{ext}[n]}{\delta n}|_{n_o} = 0. \tag{2.38}$$

Use chain rule in Eq. 2.36

$$\frac{\delta E_{ext}[n]}{\delta \psi_i^*} = \frac{\delta E_{ext}[n]}{\delta n}\frac{\delta E_{ext}[n]}{\delta \psi_i} = \frac{\delta E_{ext}[n]}{\delta n}\phi_i. \tag{2.39}$$

Combine Eq. 2.38 and Eq. 2.39

$$\frac{\delta E_{ext}[n]}{\delta n}|_{\phi} = 0. \tag{2.40}$$

Throughout the minimization lagrange multipliers are used in order to maintain the orthonormality of the Kohn-Sham orbitals [26]

$$L[\phi_1, \phi_2, ..., \lambda_1, \lambda_2] = E[\phi_1, \phi_2, ..., \lambda_1, \lambda_2] - \sum_{ij} \lambda_{ij}[\langle\phi_i|\phi_j\rangle - \delta_{ij}] \tag{2.41}$$

where $\langle\phi_i|\phi_j\rangle = \delta_{ij}$ and λ_{ij} are Lagrangian multipliers.

$$\frac{\delta L}{\delta \psi_i^*} = 0 \Longrightarrow \frac{\delta E}{\delta \psi_i^*} = \sum_j \lambda_{ij}\psi_j. \tag{2.42}$$

Insert Eq .2.37 to Eq. 2.42 and use Eq. 2.39

$$\begin{aligned} \frac{\delta E}{\delta \psi_i^*} = \Bigg(\frac{\delta}{\delta \phi_i^*}\int d^3(\vec{\mathbf{r}})\phi^*(\vec{\mathbf{r}})\frac{(-i\hbar\nabla)^2}{2m}\phi(\vec{\mathbf{r}})\Bigg) \\ +\phi_i\frac{\delta}{\delta n}\Bigg(\frac{1}{2}\int d^3(\vec{\mathbf{r}})d^3(\vec{\mathbf{r}}')\frac{n(\vec{\mathbf{r}})n(\vec{\mathbf{r}}')}{|r-r'|} \\ +\int d^3(\vec{\mathbf{r}})\nu_{ext}(\vec{\mathbf{r}})n(\vec{\mathbf{r}}) + E_{XC}\Bigg) = \sum_j \lambda_{ij}\phi_j. \end{aligned} \tag{2.43}$$

Eq. 2.43 become

$$\left[\frac{(-i\hbar\nabla)^2}{2m} + \frac{1}{2}\int d^3(\vec{\mathbf{r}})\frac{n(\vec{\mathbf{r}})}{|r-r'|} + \nu_{ext}(\vec{\mathbf{r}})n(\vec{\mathbf{r}}) + \frac{\delta E_{XC}}{\delta n}\right]\phi_i(\vec{\mathbf{r}}) = \sum_j \lambda_{ij}\phi_j(\vec{\mathbf{r}}). \tag{2.44}$$

Rearrange E.q .2.44

$$H\phi_i(\vec{\mathbf{r}}) = \sum_j \lambda_{ij}\phi_j(\vec{\mathbf{r}}) \tag{2.45}$$

$$\sum_{j}(H-\lambda_{ij})\phi_i(\vec{\mathbf{r}})=0 \tag{2.46}$$

The Lagrangian multipliers are found by determination of Eq .2.46 and let's assume hamiltonian matrix is two by two.

$$\det|H-\lambda_{ij}|=0 \quad and \quad H=\begin{pmatrix}\epsilon_1 & 0\\ 0 & \epsilon_2\end{pmatrix} \tag{2.47}$$

$$\begin{vmatrix}\epsilon_1-\lambda_{11} & -\lambda_{12}\\ -\lambda_{21} & \epsilon_2-\lambda_{22}\end{vmatrix}=0. \tag{2.48}$$

Solution of the Lagrangian multipliers $\lambda_{11}=\epsilon_1$, $\lambda_{12}=0$,$\lambda_{21}=0$ and $\lambda_{22}=\epsilon_2$. In order to find Kohn-Sham equation, insert lambda values in Eq. 2.44

$$\left[\frac{(-i\hbar\nabla)^2}{2m}+V_H(\vec{\mathbf{r}})+V_{ext}(\vec{\mathbf{r}})+V_{xc}(\vec{\mathbf{r}})\right]\phi_i(\vec{\mathbf{r}})=\epsilon_i\phi_i(\vec{\mathbf{r}}). \tag{2.49}$$

where $V_H(\vec{\mathbf{r}})=\int d^3(\vec{\mathbf{r}})\frac{n(\vec{\mathbf{r}})}{|r-r'|}$ which is Hartee potential and $V_{xc}=\frac{\delta E_{xc}}{\delta n}$ which is exchange-correlation potential.

In the end, the Schrödinger equation is replaced by a solvable expression in terms of single particle orbitals(KS orbital) in equation 2.49 which has explicit form of energy functional but the exchange correlation energy is waiting to be determined.

2.5 Local Density Approximation

So far, the formulation of the Kohn-Sham equations are exact. Simultaneous solution of the nonlinear set of equations in Eq.2.51 would, in theory, yield the solution. However, since the exchange-correlation term does not have an explicit form, this cannot be done without approximations. The simplest approximation to the exchange-correlation energy is the so-called local density approximation given by

$$E_{XC}^{LDA}[n(\vec{\mathbf{r}})]=\int n(\vec{\mathbf{r}})\epsilon_{xc}(\vec{\mathbf{r}})d\vec{\mathbf{r}} \tag{2.50}$$

where $\epsilon_{xc}(\vec{\mathbf{r}})$ is the exchange-correlation energy per electron of a homogeneous electron gas.

LDA can be is considered schematically where the system is divided into many local regions of uniform electron density with different values. Exchange-correlation energy for each region is then collected and energies in local regions are summed up to give total exchange-correlation energy. After that energies in the local regions are summed up to give total exchange-correlation energy.
Although this approximation works well with systems that have more or less uniform densities such as bulk metals, it requires improvement for systems with abrupt changes in density, such as surfaces. A better suited functional for such systems would involve, in addition to the value of the density, its spatial variation.

2.6 Generalized Gradient Approximation

For the systems mentioned above, the generalized gradient approximation(GGA) is a more accurate exchange-correlation functional. It contains both local and semi-local information.

$$E_{XC}^{GGA}[n(\vec{\mathbf{r}})] = \int n(\vec{\mathbf{r}})\epsilon_{xc}^{GGA}[n(\vec{\mathbf{r}}), \boldsymbol{\nabla} n(\vec{\mathbf{r}})]dr. \tag{2.51}$$

$E_{XC}^{GGA}[n(\vec{\mathbf{r}})]$ has no simple functional to represent correctly GGA data like $E_{XC}^{LDA}[n(\vec{\mathbf{r}})]$ has. Therefore, $E_{XC}^{GGA}[n(\vec{\mathbf{r}})]$ is expressed in terms of a function of the density $F(s)$.

$$E_{XC}^{GGA}[n(\vec{\mathbf{r}}), s] = \int n(\vec{\mathbf{r}})\epsilon_{xc}^{GGA}[n(\vec{\mathbf{r}})]F(s)dr. \tag{2.52}$$

s depends on electron density and it's gradient

$$s = C\frac{|\boldsymbol{\nabla} n(\vec{\mathbf{r}})|}{n^{\frac{4}{3}}(\vec{\mathbf{r}})}. \tag{2.53}$$

The typical range of electron density is s equal to $0 - 3$ in solids. In this range, GGA and $F(s)$ exchange typically vary 1.0 and 1.6. Therefore, GGA has many different form which are most important ones are PW91 [28] and PBE [27].

2.7 Hybrid functionals

Both functionals mentioned above suffer from the well-known "band gap" problem, where they underestimate the band gap of semiconducting materials. As a remedy

of this problem, hybrid exchange-correlation functionals have been proposed. Several formulations for hybrid functionals are in common use such as PBE0, HSE and B3LYP which give more sufficient and accurate exchange-correlation energy.
The hybrid functionals are function with GGA-type functional and accurate exchange energy form Hartee-Fock method. PBE0 functional is formulated by

$$E_{XC}^{PBE0} = \frac{1}{4}E_X + \frac{3}{4}E_X^{PBE} + E_C^{PBE}. \tag{2.54}$$

The B3LYP [Stephenes et al 1994] functional includes three parameters where EX represents exact exchange calculated within the HF treatment, E_x^{PBE} and E_c^{PBE} are the PBE exchange and correlation energies, respectively. It is very popular in molecular chemistry because it describes the systems with long-range interaction(Van-der Walls) accurately and efficiently. It is also useful in calculation of band energies and band gap.

$$E_{XC}^{B3LYP} = 0.19E_X^{VWN3} + 0.81E_C + 0.72E_X^{LYP}. \tag{2.55}$$

Where E_X^{LYP} is Lee, Yang and Parr [29] correlation energy which contains semi-local and local part and E_C^{VWN3} is local Voska-Wilk-Nusair [30] correlation functional three which is filled to the correlation energy in the random phase approximation of homogeneous gas.
The other important functional is the Heyd-Scuserin-Ernzerholf [31] which is used as an error function to calculate the exchange spare of energy for improving computational performance, particularly for metallic system

$$E_{XC}^{HSE} = \alpha E_x^{HF,SR}(\mu) + (1-\alpha)E_x^{PBE,SR}(\mu) + E_X^{PBE,LR}(\mu) + E_c^{PBE}(\mu). \tag{2.56}$$

Where α is a mixing parameter between the short range PBE energy $E_x^{PBE,SR}(\mu)$ and the short range HF exchange energy $E_x^{HF,SR}(\mu)$ and μ parameter defines range separations which are negligible at short range interactions.

2.8 The van-der Waals Interaction

Standard DFT does not include long-range dispersion because the exchange-correlation term V_{xc} is defined with only local electron density. Therefore standard DFT can not model correlation outside the Fermi Hole [32]. To fix this problem, various approaches have been derived and one of them is DFT-D [33] . In this method, an empirical, London-style correction is added to the ground state energy of the system to account for dispersion. The latest version of this approach is DFT-D3

$$E_{DFT-D3} = E_{DFT} + E_{disp} \tag{2.57}$$

Eq. 2.57 defines the total energy. E_{DFT} is the usual self-consistent Kohn-Sham energy and E_{disp} is dispersion correction as a sum of three-body and two-body energies, where

$$E_{disp} = \sum_{AB} \sum_{n=6,8,10,..} s_n \frac{C_n^{AB}}{r_{AB}^n} f_{d,n}(r_{AB}). \tag{2.58}$$

Where C_n^{AB} is nth-order dispersion coefficient for atom pair AB, r_{AB} is distance between of AB and s_n is scaling factor.

$f_{d,n}(r_{AB})$ is defined as a damping function . Because, DFT-D methods can reach singularity in the short distance interaction, damping function[damping] is needed to eliminate them for small interfragment

$$f_{d,n}(r_{AB}) = \frac{s_n r_{AB}^n}{r_{AB}^n + (a_1 R_{0AB} + a_2)^n}. \tag{2.59}$$

Where $R_{0AB} = \sqrt{\frac{C_{8AB}}{C_{6AB}}}$ and s_n is the scaling factors used for the repulsive behaviour of the chosen exchange-correlation density functional. The parameters a_n are adjusted manually such that the dispersion correction is smaller than one percent of maximum dispersion energy for typical covalent bond distances.

CHAPTER 3

RESULT AND DISCUSSION

In this section interaction and friction behaviour at interfaces between molybdenum disulfide and high symmetry surface of gold will be investigated. In particular, our calculations represent an experimental scenario where a Au-coated AFM tip is used to probe a 2D MoS_2 film. With the typically large diameter of AFM tips as compared to the atomic bond lengths, the AFM tip is modeled by a perfect Au(111) surface. In order to construct periodic interfaces of molybdenum disulfide and gold, proportional unit cells must be identified that do not cause overstrain in either material.

After proper cell configurations were constructed, the lateral sliding calculations of the molybdenum disulfide layer on Au surfaces along the x-direction and y-direction were conduct under different magnitudes of load. Surface cell separated by at least a 18 Å vacuum was used to simulate the sliding model. Total energy was converged up to 10^{-5} eV for electronic relaxations.The long range interaction of the interface is examined with vdW-DF3. All internal coordinates were relaxed until the Hellmann–Feynman forces were less than 10^{-4} eV/Å to optimize geometries with conjugate gradient algorithm. The electronic band structures are constructed by HSE06 and PBE-D3 functionals with Gaussian smearing . Density state calculation of MoS_2 structure studied with using PBE [27] . The charge density differences of the interface are calculated with using DFT-D3 [33]. The each calculations are done with projector-augmented wave(PAW) method [34] [35] and are simulated with Vienna *ab initio* simulation package(VASP) [36] [37] .

3.1 Preliminary Calculations

3.1.1 Molybdenum disulfide

In order to confirm the calculation parameters chosen for simulations, the lattice constant of the MoS_2 calculated using PBE.The unit cell used for these calculations and the variation of total energy as a function of lattice parameter is shown in Fig. 3.1a The cut off energy of the plane-wave basis was 400 eV and a 13 x 13 x 1 mesh is used for Brillouin zone integration. The calculated value is 3.18 Å which is in very good agreement with experimental results of 3.16 Å [38] , 3.27 Å [39] .

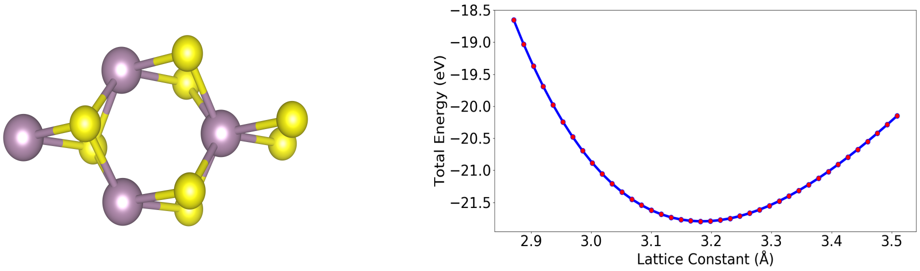

(a)

(b)

Figure 3.1: (a) MoS_2 structure.(b)Energy versus lattice constants for MoS_2 structure

After the construct a proper unit cell of the MoS_2, electronic structure of MoS_2 are examined with PBE functional. The Brillouin zone(BZ) was hexagonal. Therefore IBZ path was chosen $\Gamma - K - M - \Gamma$. The corresponding energy bands is showed in 3.2. Optical band gap value was 1.67 eV on K point of the IBZ which has good agreement recent PBE studies [40] [41] . The orbital structure of Molybdenum is $4d^5$ $5s^1$ and S is $3s^2$ $3p^4$ so we expected to observe the last occupied state which is closet to the Fermi level is constructed mostly by the $4d$ orbital of Molybdenum as shown in the density of states plot figure 3.2 and consistent with previous studies [42].

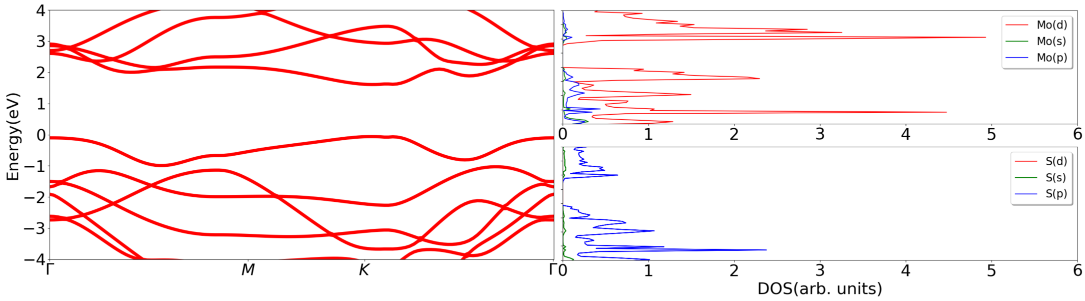

(a)

(b)

Figure 3.2: (a) Band structure of monolayer MoS_2.(b) DOS of MoS_2 single layer

The phonon dispersion of MoS_2 calculated by small- displacement method [43] with using 4x4 supercelland by means of solving the secular equation $\left|\frac{C_{ia,jb}(q)-\omega^2}{\sqrt{m_i m_j}}\right| = 0$ here q is the wave-vector, m_i, m_j are the atomic masses of atoms i and j. The dynamical matrix is defined as $C_{ia,jb}(q) = \frac{\partial^2 E}{\partial c_i \partial c_j}$.

The result of phonon dispersion calculation shown as figure 3.3 and result is in good agreement with calculation of lattice dynamics of MoS_2 [44]. There is an almost non-dispersive phonon at 12 THz which is called homopolar mode and this mode is characteristic for layered structures. This mode corresponds to a change in the layer thicknes .

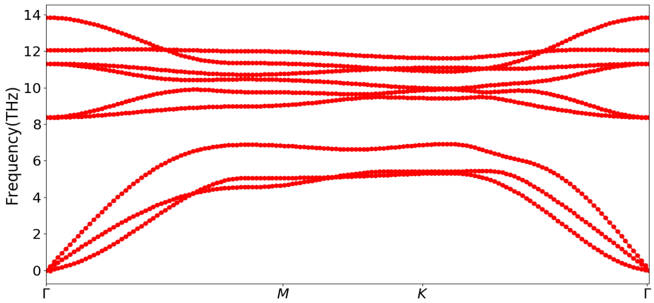

Figure 3.3: Phonon dispersion curves of MoS_2 layer.

3.1.2 Hybrid Functional of MoS_2's band structure

In this section, electrical properties of MoS_2 is calculated using hybrid. As mentioned, GGA and LDA are not suitable to calculate band gaps of semiconductors due to lack of exact Hartee-Fock exchange energy. The hybrid Heyd-Scuseria-Ernzerhof functional includes Hartee-Fock exchange energy for short range interaction and give yields a parametrically band gap value that matches the experimental value.

The HSE06 band gap is 2.14 eV when calculated with a mixing paramater (alpha) of 0.25 (See Equation 2.56 above for a definition). To approach the experimental value of 1.90 eV even more, we repeat the calculation with an alpha of 0.1. This gives the much more accurate band gap of 1.88 eV.

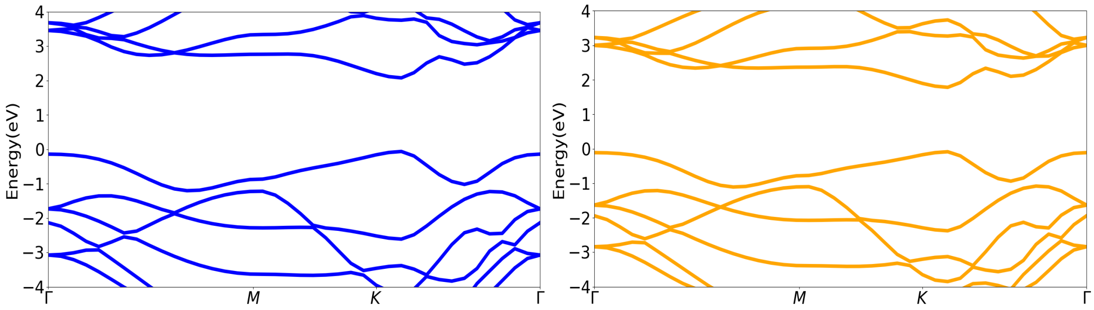

(a)

(b)

Figure 3.4: (a) Band structure of monolayer MoS_2 with HSE06($\alpha = 0.25$).(b) Band structure of monolayer MoS_2 with HSE06($\alpha = 0.1$)

3.1.3 Au Bulk Structure

Before constructing our production simulation cells with the Au(111) surface, we test the DFT-D3 functional with Au bulk. Although normally Au does not require van der Waals corrections due to the metal bonds, therefore it is important reproduce the usual behavior of this component also within the DFT-D framework. To this end, we calculate the lattice constant and find 4.1012 A, in very good agreement with 4.0782 A [45]. The energy versus lattice constant data is displayed in Fig. 3.5

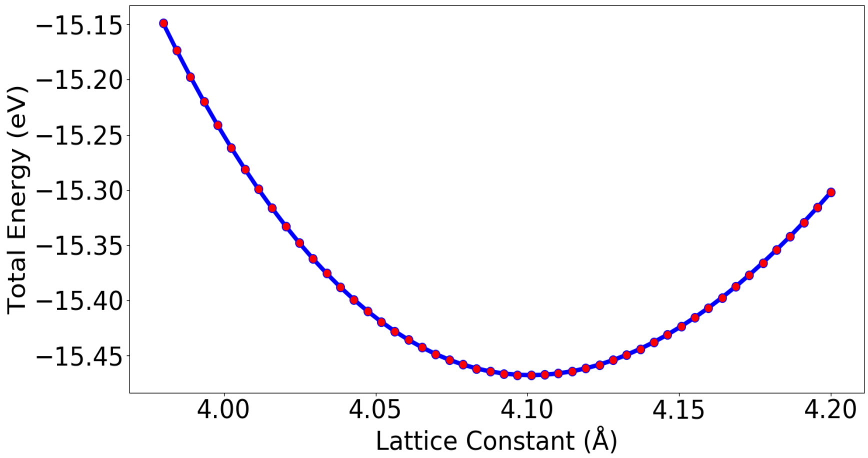

Figure 3.5: Total energy vs lattice constant of bulk Au.

3.2 The MoS_2/Au(111)

3.2.1 Finding an appropriate simulation cell

In this section, we construct molybdenum disulfide layer and Au(111) surface in the same simulation cell in order to map their joint PES. In order to conduct this kind of a study in a reasonably sized system, strain must be introduced to one or both components. Materials are expanded or compressed depending on their lattice parameters. The Au(111) surface's lattice parameters $\vec{a} = 5.52\ \hat{x}$ Å , $\vec{b} = 9.73\ \hat{y}$ Å and MoS_2's $\vec{a} = 5.46\ \hat{x}$ Å , $\vec{b} = 9.45\ \hat{x}$ Å. We prefer to expand MoS_2's lattice parameters. The resulting unit cell for this interface is shown in Figure 3.6 . The strain necessary for fitting both materials into a reasonable simulation cell is well within the range of acceptable strains used in similar works [46]

The internal geometry optimization was calculated for Au(111) surface and MoS_2 sheet configuration. The four layer of Au(111) were moved freely in three axis but the fist two bottom layers were fixed in all coordinates to act as a bulk. The MoS_2 sheet moved freely with last four layer of Au(111) in all coordinate. After this configuration was set, relaxation process was simulated. Corresponding to minimum interaction energy for this simulation was calculated using

$$E_{int} = E_{tot} - (E_{Au} + E_{Mos_2}) \tag{3.1}$$

Table 3.1: Percentage strain for adjustment of Au(111) and MoS_2 surface unit cell

Structure	Initial lattice parameter	Final lattice parameter	Strain(%)
MoS_2 x-axis	5.46	5.52	1.82
Au(111) x-axis	5.52	5.52	0
MoS_2 y-axis	9.45	9.73	2.88
Au(111) y-axis	9.73	9.73	0

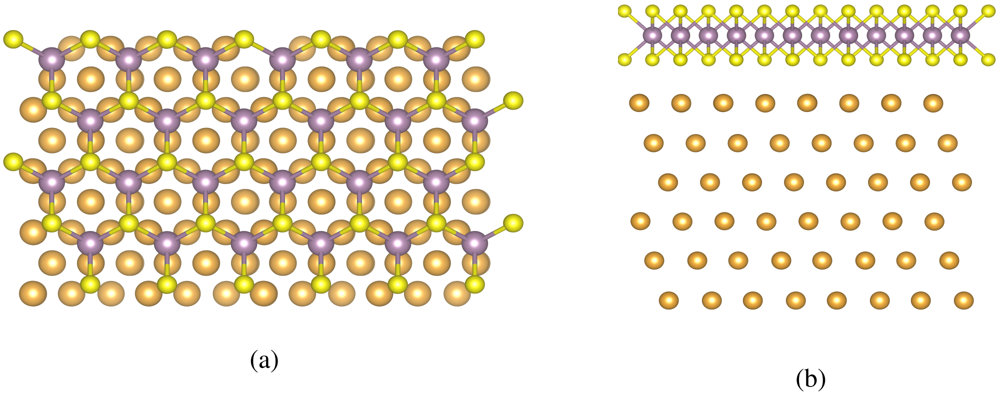
(a)

(b)

Figure 3.6: (a)MoS_2 and Au(111) unit cell configuration on side view and (b)MoS_2 and Au(111) unit cell configuration on side view

where E_{tot} is total energy, E_{Au} is the energy of layers Au interface and E_{MoS_2} is energy of one MoS_2 layer.

The MoS_2 layer initially position hollow side on the Au(111) layer. Neither Mo and S were positioned on top of Au atoms as shown in figure 3.7 .

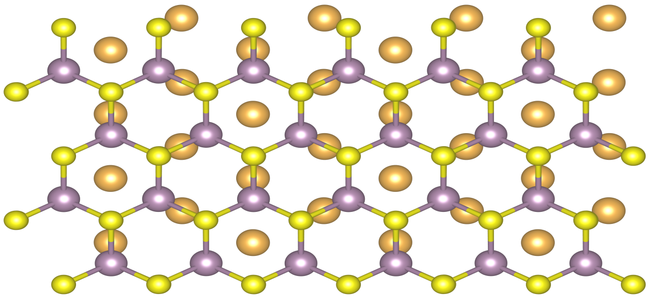
Figure 3.7: The configuration of top layer of Au(111) and MoS_2 layer

The k-point mesh was set to 12 x 7 x 1 for mutual unit cell and DFT-D3 method with Becke-Jonson damping is used, while the Perdew–Burke–Ernzerhof (PBE) functional was employed to describe the exchange and correlation effect equilibrium interface separation corresponding to equilibrium distance was calculated to be $d_{eq} = 2.784$ Å and minimum energy was $E_{KS+disp,min} = -201.937\ meV/MoS_2$. When electron correction is not considered , there is a only KS energy at interface interaction which was $E_{KS} = -43.94\ meV/MoS_2$ for distance $d_min = 3.459$ Å and interface never found global minimum energy configuration as shown figure .3.8 . These results are consistent with equation 2.57 .

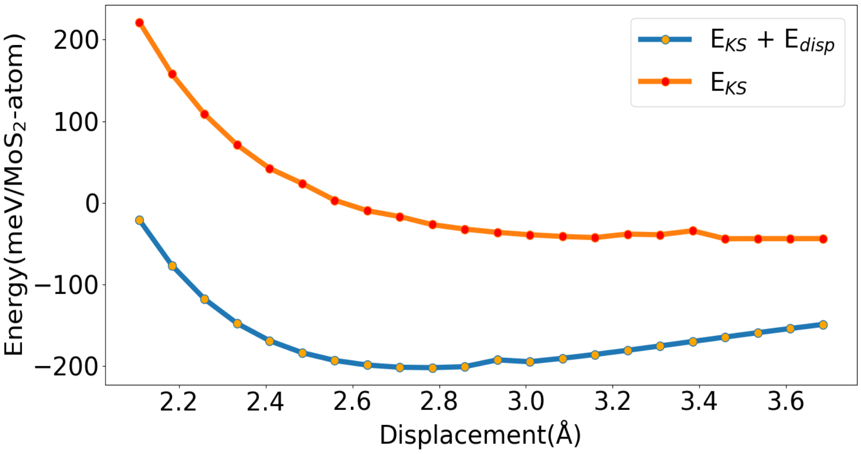

Figure 3.8: Equilibrium separation distance and interaction energy between MoS$_2$ layer and Au(111) surface

Before the examination of force effect and load properties of the Au(111) and MoS$_2$ structure, electronic interaction between the interface is calculated so that help to clearly understand of tribological behaviour. The charge distribution due to interface adsorption can be characterized by the charge density difference(CDD). The CDD was found by $\delta\rho = \rho_{total} - \rho_{MoS_2} - \rho_{Au}$ where ρ_{total}, ρ_{MoS_2},ρ_{Au} represent the charge density of the system. There is an electron transfer between interface and the electron accumulation around the Au atoms is carried out by electron depletion of sulfur atoms. In this transfer weak van der Waals interaction play a leading role as shown figure 3.10 . When van der waals energy did not included to interface interaction, planar charge density value decrease almost % 60 for each grid at the interface . Moreover, charge density accumatiton and deplotion between Au layers more apparent at the interface which has no vdW energy as shown figure This interaction can take a role to slide mechanism for the interface and we will examine it in following chapters.

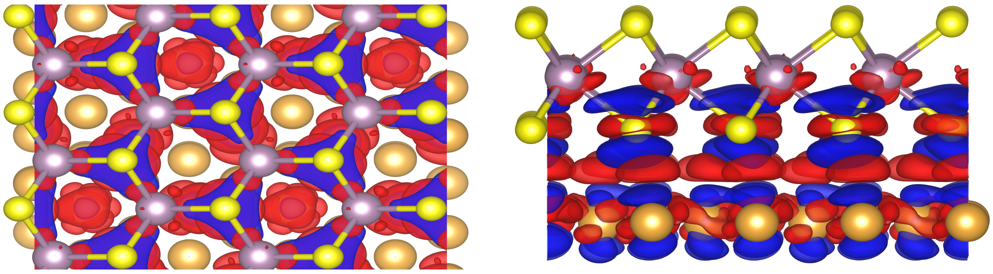

(a)

(b)

Figure 3.9: (a)Top side of interface and (b)side view of interface. The red and blue isosurfaces represent to positive and negative charge difference with isosuface 0.0006

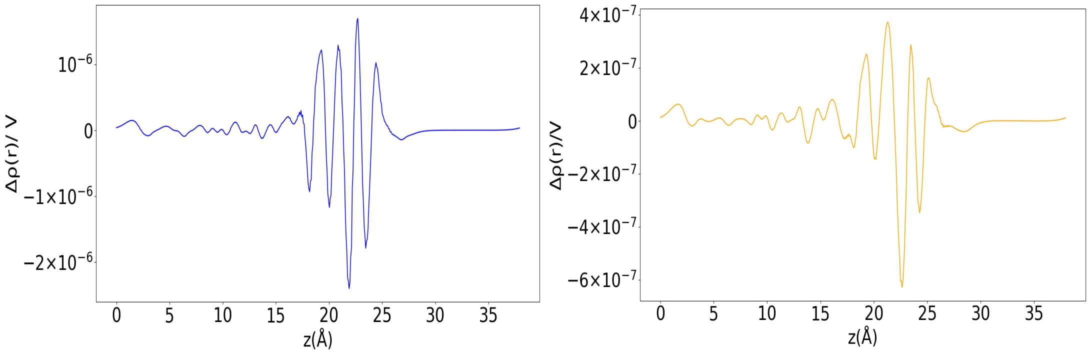

(a)

(b)

Figure 3.10: (a)Average charge density of the interface which has vdW energy along z axis (b)Average charge density of the interface which has no vdW energy along z axis

3.2.2 Load Dependence of Energy and Friction Force

In this section we investigate friction forces as a function of load along a sliding path in the x-axis and y-axis direction. We consider MoS_2 layer and Au(111) surface of the same rectangular unit cell in relative motion where the spacing z between top layer of Au(111) surface and bottom plane of MoS_2 is fixed to a series of values. To examine the tribological behaviour of this system, friction forces' pattern of structure on the different magnitudes of load is studied potential energy of surface is calculated to reveal the mechanics of tribological behaviour and charge density difference is examined at relative positions for understanding the relationship between the friction force and electronic properties of the interface. Initial and final positions along the x- and y-direction sliding paths are shown in 3.11 .

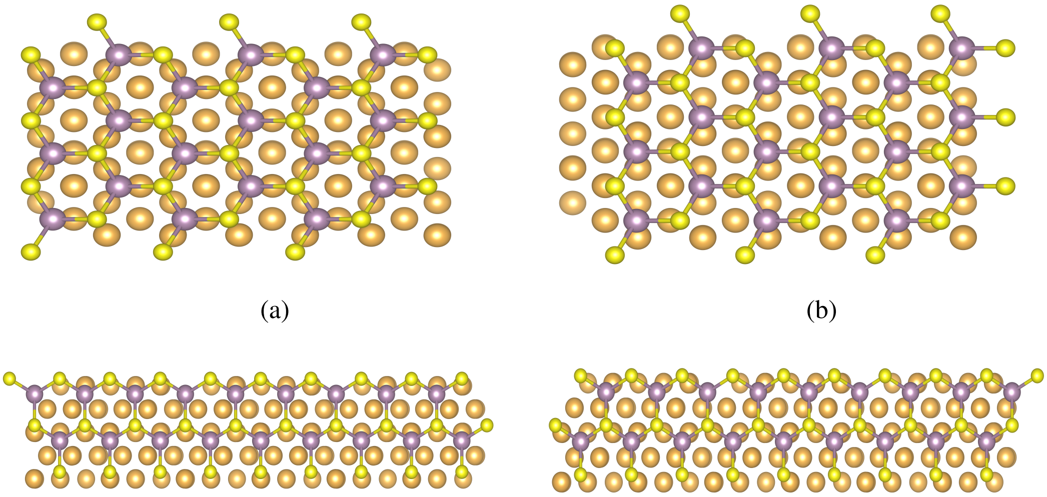

(a) (b) (c) (d)

Figure 3.11: Lateral displacement sites of MoS_2/Au(111) interface (a)displacement 0 Å in x-axis. (b)displacement 0.4 Å in x-axis. (c) displacement 0 Å in y-axis. (d) displacement 0.6 Å in y-axis

The lateral force on the top layer of the Au(111) surface is calculated from the gradient of the total energy of the Au(111)-MoS_2 system using is $\vec{\boldsymbol{\nabla}} E_T(x, y, z) = -\vec{\mathbf{F}}(x, y, z)$. The atomic forces for top layer of Au(111) surface is calculated with Hellman-Feynman theorem. Since directly constraining the vertical load is not possible in our calculation, we find the behavior of the lateral friction force for each load through an interpolation scheme. The normal force is derived from $F_z(x, y, z) = -\frac{\partial}{\partial z} E_T(x, y, z)$ and the value of z where $F_z(x, y, z) = F_{z0}$ is calculated for each x and y. The vertical distance that yields a particular load as a function of x and y can be displayed as $z_0(x, y)$ parameters. $F_{x_0}[x, y, z_0(x, y)]$ and $F_{y_0}[x, y, z_0(x, y)]$ which are x and y dependence of the lateral force is calculated by using spline interpolation in the z direction.

When the normal Force F_{z_0} is increased on the Au(111) surface friction force shows an increasing trend according to the results that can be seen at figure 3.12 .

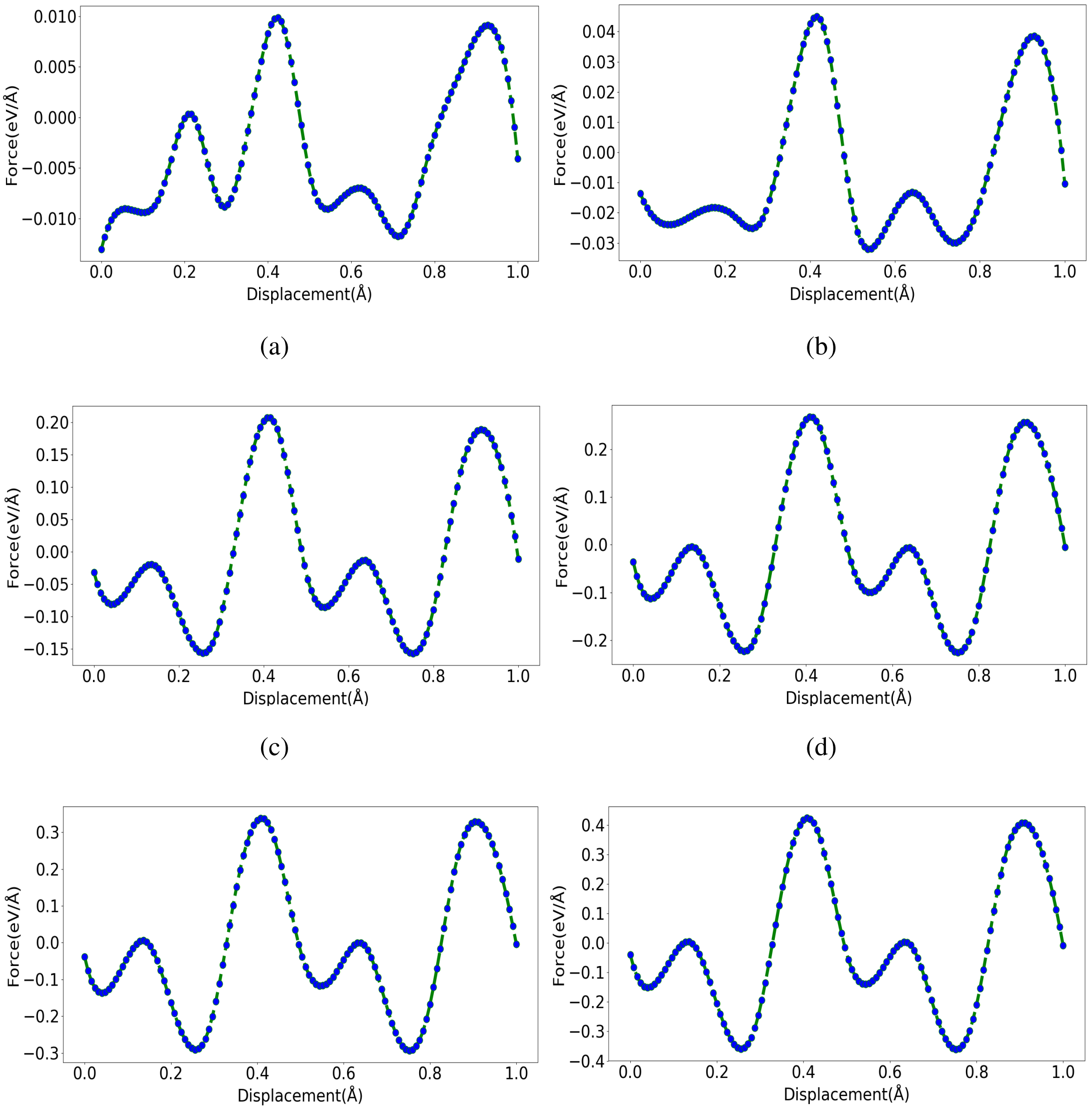

(a) (b)

(c) (d)

(e) (f)

Figure 3.12: lateral friction force of vertically loaded Au(111)-MoS$_2$ structure in several orders in x direction.(a) 0 eV Load.(b) 2 eV Load.(c) 8 eV Load. (d)10 ev Load. (e) 12 eV Load. (f) 14 eV Load .

As the magnitude of normal load increase, it is observed that value of potential wells increase in both direction . According to Figure 3.12, there is one global minimum point at the loads 2 eV Å but after it, potential barrier at 0,25 Å become a global minimum point with another potential barrier at 0,78 Å. On the other hand, there are

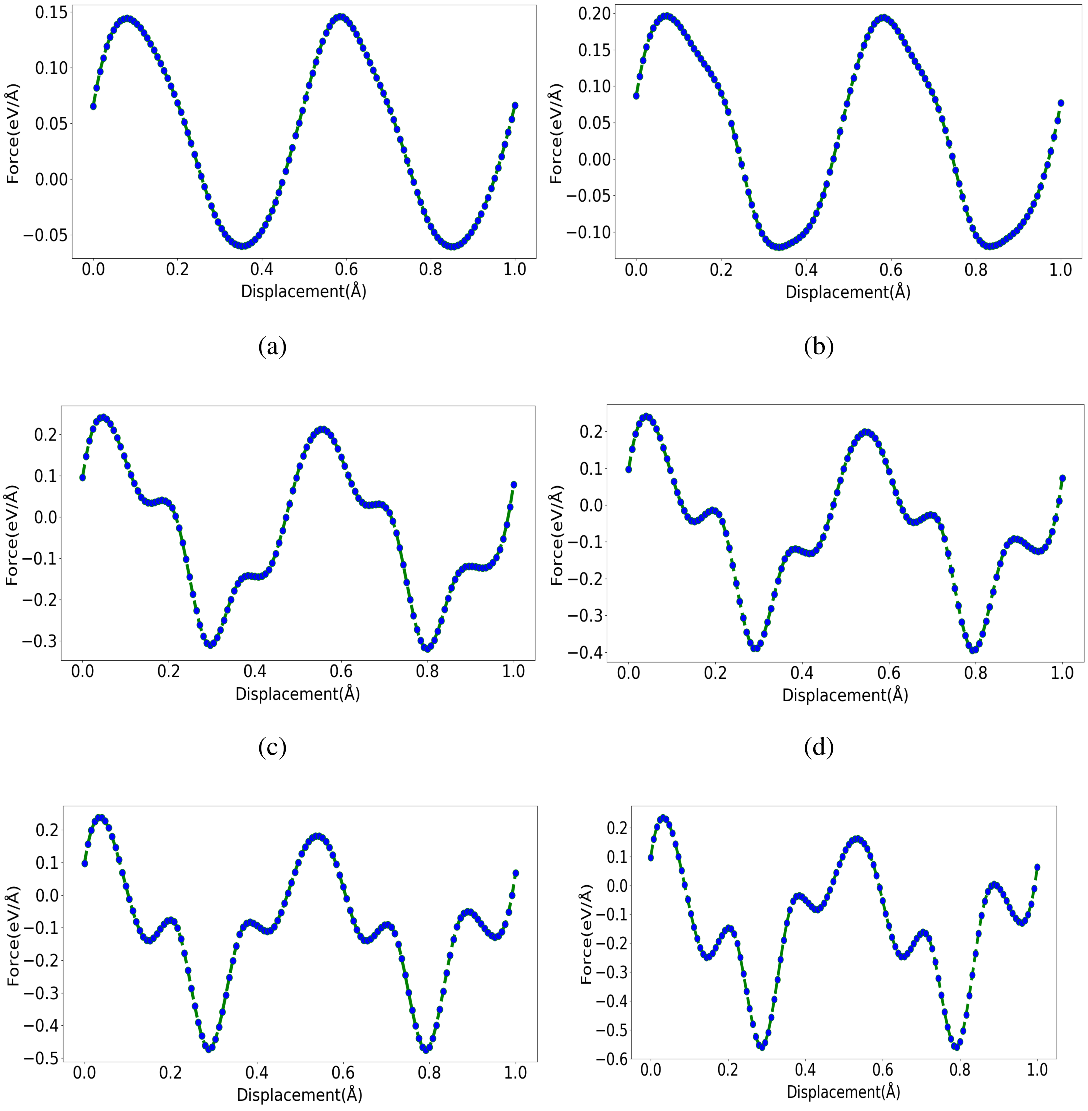

(a) (b)

(c) (d)

(e) (f)

Figure 3.13: Lateral friction force of vertically loaded Au(111)-MoS_2 structure in several orders in y direction .(a) 0 eV/Å Load.(b) 2 eV/Å Load.(c) 8 eV/Å Load. (d)10 eV/Å Load. (e) 12 eV/Å Load. (f) 14 eV/Å Load .

always two global minimum points for each loads in y direction. When magnitude of normal load increase, value of the potential barriers. Moreover, there is a different depth between the barriers for each magnitude of normal load due to sandwich structure of MoS_2 and asymmetric Au surface in both direction. For the smallest loads of 0 and 2 eV Å the behavior is almost sinusoidal. When the load increases to 8 eV Å and above, small local minimum points begin to occur. The magnitude of the forces display an overall increase at both direction as the load increases as expected due to the increasing electron density overlap. Moreover, we visualized position of MoS_2 structure for each vertical load in base position of sulphate atom which use as a index in sliding shell script shown figure 3.14 . The each vertical load, the interface has furthest distance for position of z at 0.3 and 0.85 Å x axis. This regions probably have most interaction energy than other sliding path

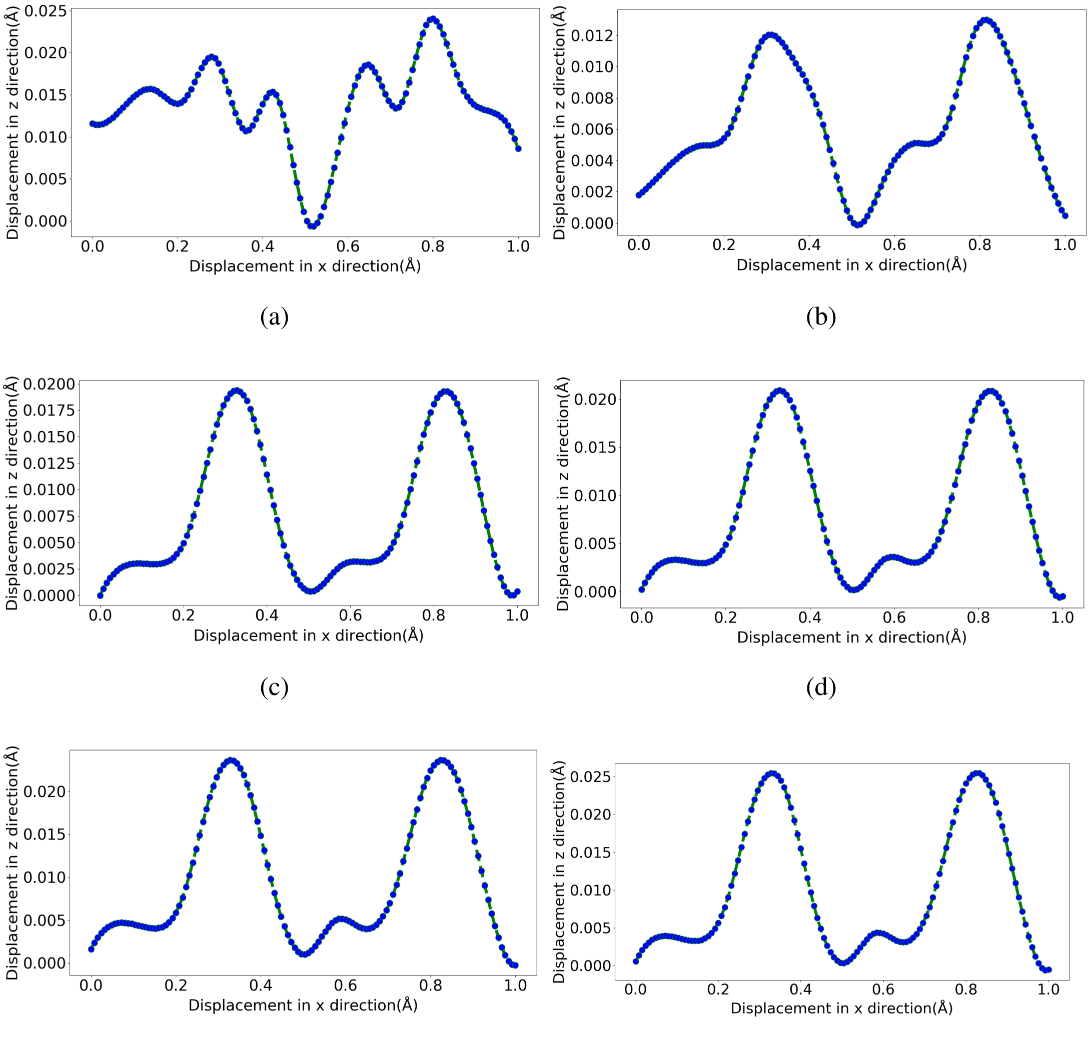

(a) (b)

(c) (d)

(e) (f)

Figure 3.14: Position of MoS_2 structure in x axis versus z axis .(a) 0 eV/Å Load.(b) 2 eV/Å Load.(c) 8 eV/Å Load. (d)10 eV/Å Load. (e) 12 eV/Å Load. (f) 14 eV/Å Load .

Result from six different loads for both friction coefficient(μ) and average lateral force were calculated in Eq. 3.2 and were examined as can be seen in fig. 3.15 and 3.16. The average of the lateral forces over the sliding direction is calculated

$$F_x = \frac{1}{N} \sum_{i=1}^{N} F(x_i) \tag{3.2}$$

$$F_y = \frac{1}{N} \sum_{i=1}^{N} F(y_i). \tag{3.3}$$

This formula is applied when $F(x_i) < 0$ and $F(y_i) < 0$.which means that only lateral forces that are against the direction of travel is taken into account for these calculations. N is the total force number which included in this sum.

The static friction coefficient is calculated with standard procedure

$$\mu = F_L/F_N \tag{3.4}$$

Where F_L is lateral force in x or y mesh and F_N is load in the z direction.

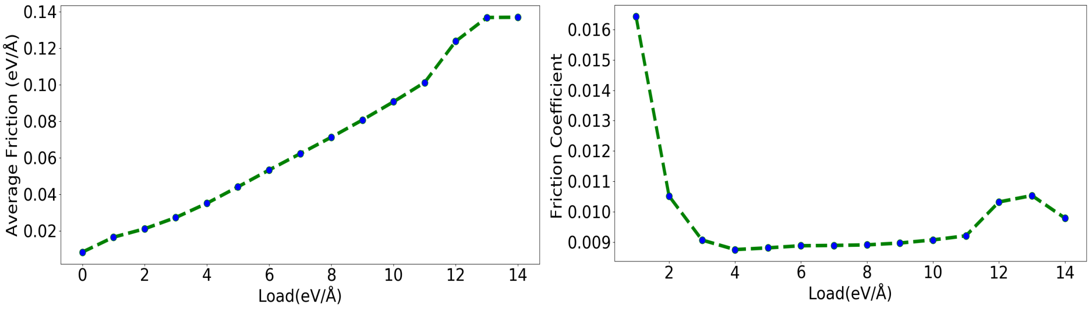

(a)

(b)

Figure 3.15: (a) Average lateral friction force (b)friction coefficient with increasing applied load over MoS_2-Au(111) interface configuration in x direction sliding path

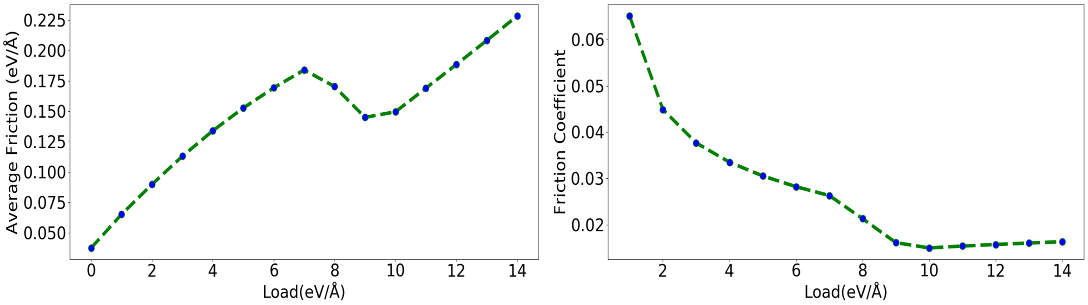

(a) (b)

Figure 3.16: (a) Average lateral friction force (b)friction coefficient with increasing applied load over MoS_2-Au(111) interface configuration in y direction sliding path

As the magnitude of normal load increase, average friction force shows a increasing trend in both sliding path. In the x direction, average force increase linearly until 11 eV/Å load. Then, between $11 - 14$ eV/Å, average force increase slightly. In the last part of the graph, there is a horizontal tangent line between $12 - 13$ eV/Å. On the other hand, average force in y direction has linearly increasing trend between $0 - 7$ eV/Å load. Then, it decrease until 9 eV/Å after that increase linearly. The friction coefficient display a parabolic decreasing trend until 4 eV/Å in x direction. It display increase trend almost linearly until 11 eV/Å load and between $11 - 13$ eV/Å load, it shows a parabolic increasing trend. The friction coefficient in y direction display a parabolic decreasing trend until 7 eV/Å and between $7 - 10$ eV/Å loads, it showed almost linearly increasing trend. In the end, it display a slightly increase trend. These friction coefficient trends show that MoS_2 layer faced more lateral friction force in each load when it was sliding along x-direction than y-direction.

To shed light on increasing trends of friction coefficients, we calculated average linear charge density at four special points for x direction, we chose 4 eV/Å vertical load which was begging point of increasing trend, 10 eV/Å vertical load which was almost end of the linearly increasing trend and 14 eV/Å, 12 eV/Å vertical loads which were maximum points of increased trend. When vertical load increased on structure, charge accumulation and depletion on Au atoms at top of layer and the interface increased as shown figure 3.17. This charge distribution increased to coulomb forces then friction coefficient of the interface increased due to attractive forces between the interface.

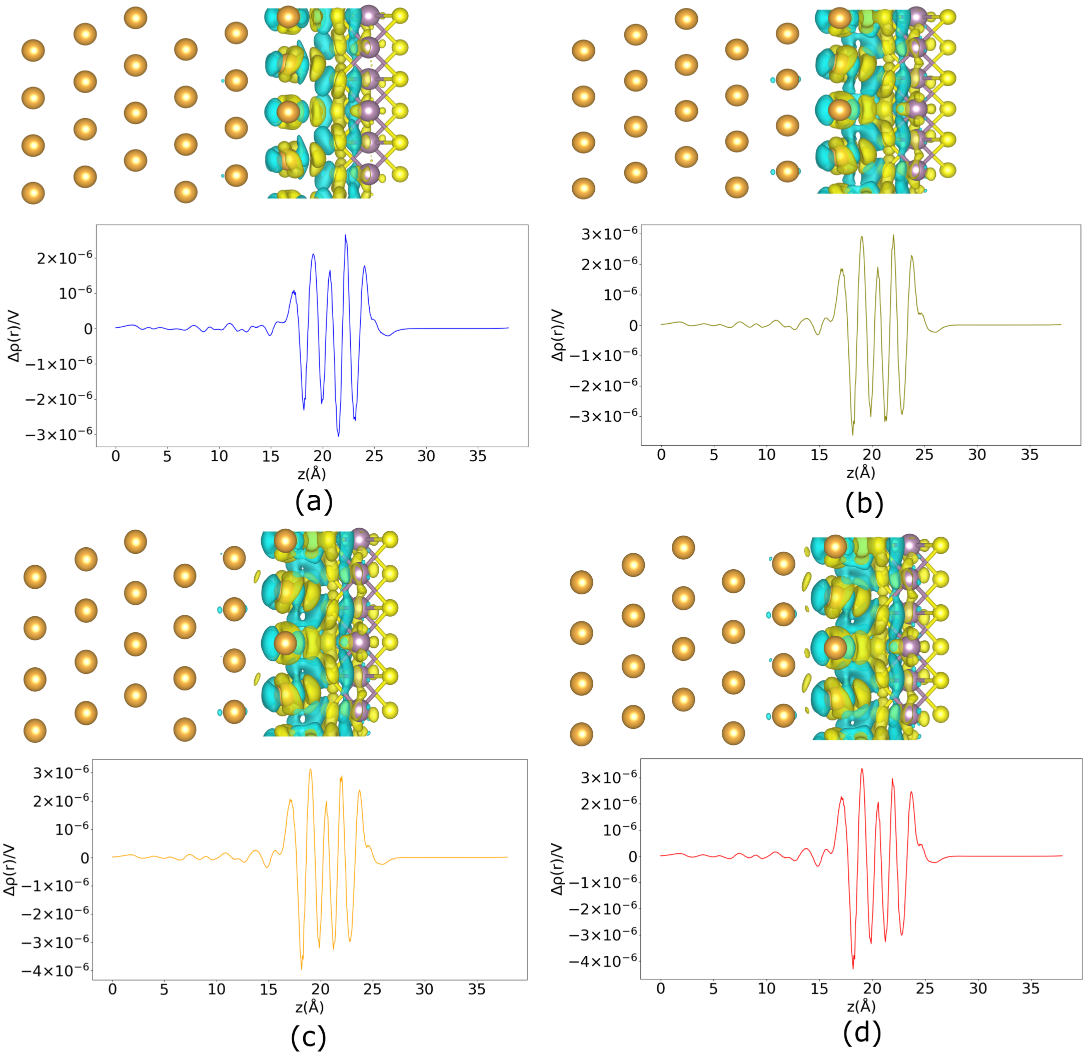

Figure 3.17: Isosurfaces and variation of linear density of charge density difference along z-axis.(a) $4\ eV$/Å Load.(b) $10\ eV$/Å Load.(c) $12\ eV$/Å Load. (d)$14\ eV$/Å Load.

So far we analysis the surface profile along the x and y axis. This, however, assumes that the MoS_2 layer is constrained to move along a straight line without being allowed to wander sideways as it slides. While this presents a useful upper limit to the friction coefficient, this restriction must be lifted for a fuller understanding of the behavior. Therefore, potential surface energy(PES) is calculated for $Au(111)/MoS_2$ interface. To obtain the PES, we form an 10 by 10 in the rectangular simulation cell and scan this mesh by means of positioning the MoS_2 layer at the grid points. We then compute a realistic optimization calculation by means of fixing the Mo atoms of the MoS_2 layers in the xy plane and allowing all other MoS_2 degrees of freedom to move during optimization. This allows us to prevent sideways sliding during force minimization. The energy corrugation was 0.94277778 $meV/atom$ between maximum energy point A and minimum energy point B which are shown in figure 3.18 Moreover, we calculated minimize energy for point A, B and C without dispersion energy. The energy corrugation was 0.02090 $meV/atom$ between point A and point B. Result show that the interface has more smooth path even between minimum and maximum energy points without long range dispersion and in this situation, we could not observe friction behavior to fit in real space interaction of structures case.

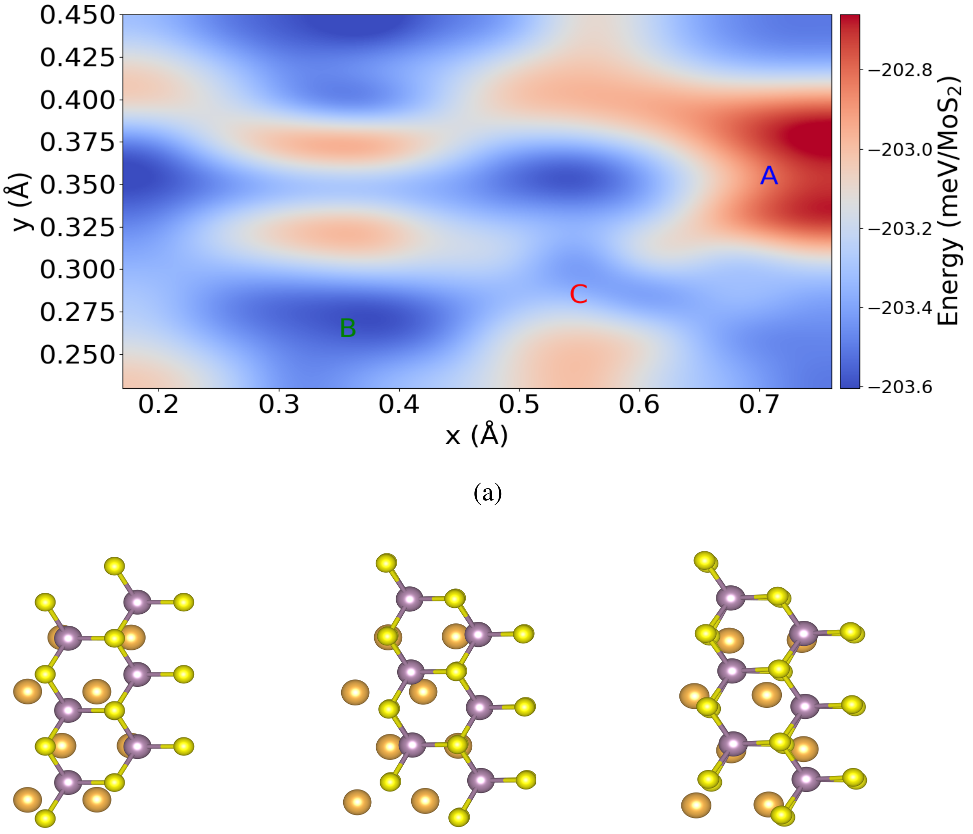

(a)

(b)

(c)

(d)

Figure 3.18: (a)The potential surface calculation graph of $Au(111)/MoS_2$ with labels.(b) Label A configuration.(c) Label B configuration. (d)Label C configuration.

The C point is a saddle point of the interface. This point is very important because one well to the adjacent one requires to overcome the barriers at these points. The interface will take the path which should include saddle point by arrows to minimize energy dissipation during the sliding as shown figure 3.19.

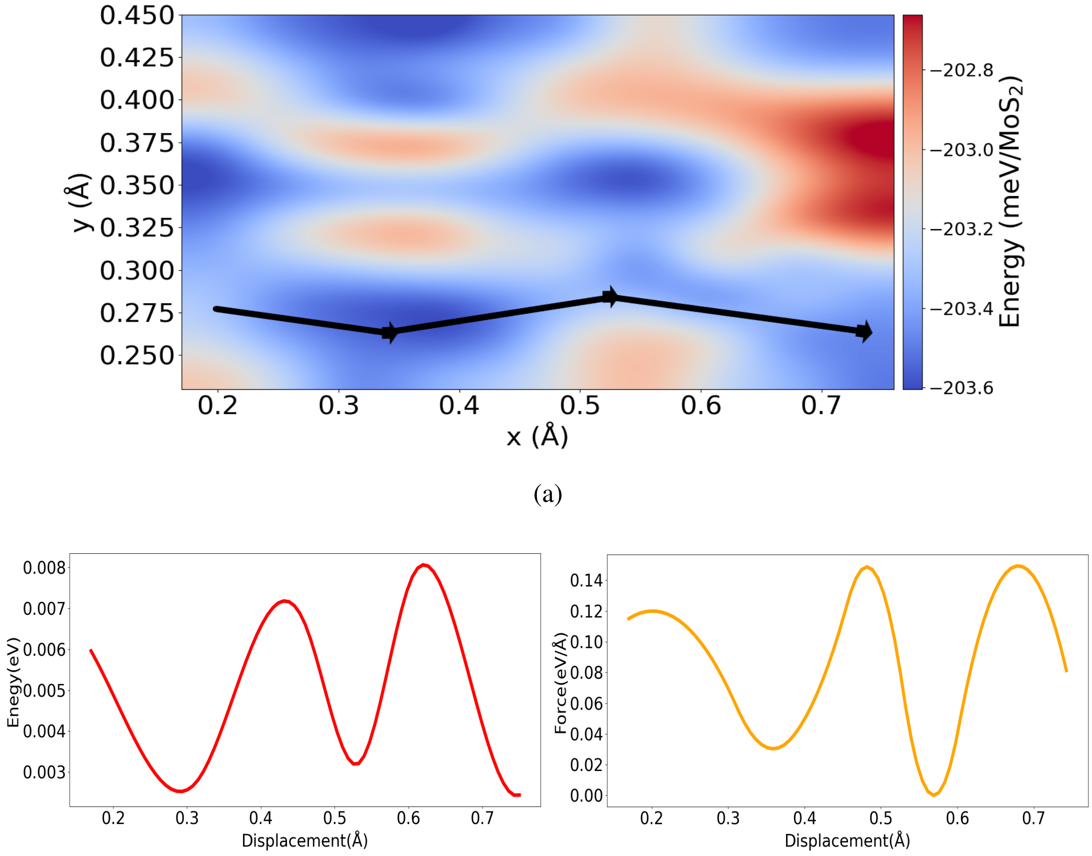

(a)

(b)

(c)

Figure 3.19: (a)The potential surface calculation graph with minimum energy path.(b) Energy versus displacement.(c) Force versus displacement.

MoS_2 structure structure along the straight line passing through two wells, saddle point and one hill as shown figure 3.19b . The energy corrugation of this path is $0.00533\ meV/atom$ which 99.4 percent lower than energy peak of PES. We note that the lateral force along this path is calculated using numerical derivative.

$$E'(x) = \frac{E(x_i) - E(x_{i+1})}{x_i - x_{i+1}}. \tag{3.5}$$

From definition of force and energy relation $F(x) = -\boldsymbol{\nabla} E(x)$, force values as shown figure3.19c. The critical stiffness of well one is $1.2901308\ eV/\text{Å}^2$ and well two is

$4.4351962\ eV/\text{Å}^2$. The intrinsic stiffness value is $2.812696\ eV/\text{Å}^2$. The slip-stick behavior is observed at well-two region.

To shed light into friction behavior of the interface,the self-consistent charge density difference was examined in saddle, max and min point of potential surfaces. The charge density difference is expressed as $\Delta\rho = \rho_{total} - (\rho_{Au} + \rho_{MoS_2})$ and the planar-averaged density is calculated along the z-direction. There is no significant difference on linear charge density at these points. Therefore we studied on max point of PES calculation to explain charge transfer on the interface as shown figure 3.20.

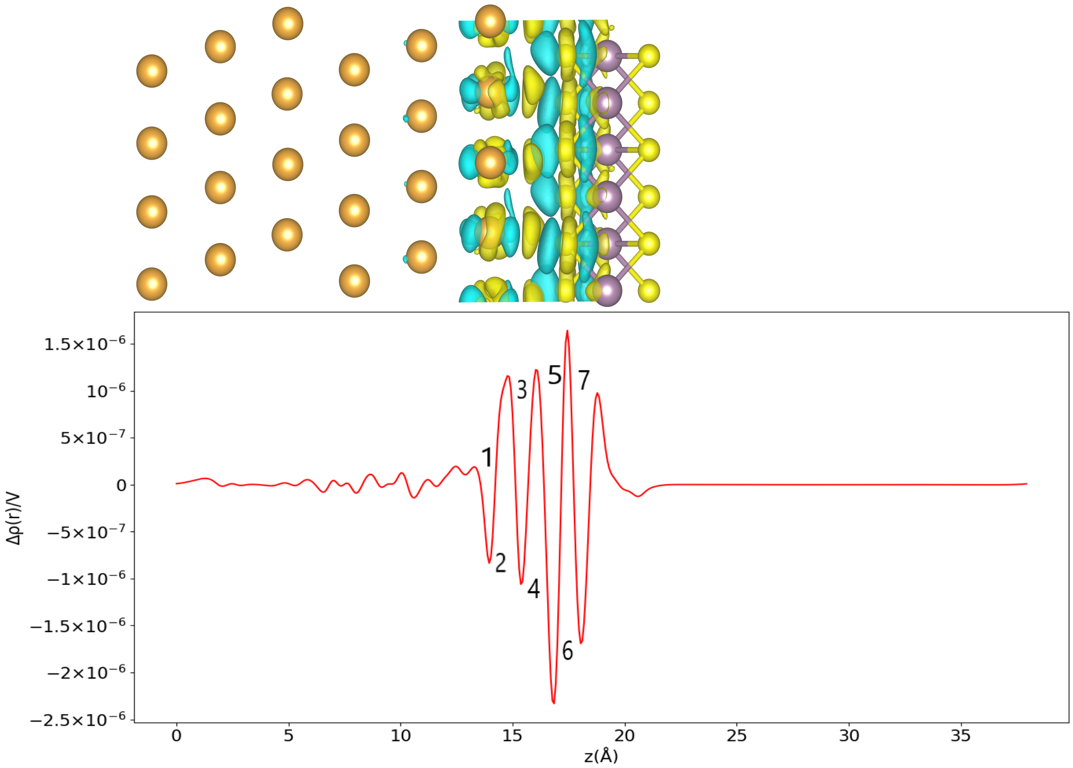

Figure 3.20: Isosurfaces and variation of linear density of charge density difference long z-axis on max point of PES. Blue isosurfaces plots correspond to the charge density depletion, yellow one correspond to accumulation and isosuface is 0.0006

The numerals 1 in linear charge density plot corresponds to a charge depletion between fifth layer and top layer of Au slab due to coating of MoS_2 surface. The charge density transfer in numeral 4 and 5 in linear charge density difference may be the key feature to explain interaction of interface. In the numeral 4, there is a charge accumulation due to top layer of Au slab. Moreover, there is a charge depletion in numerical 5 which is more than charge density of accumulation. The main factor of this magic is vdW interaction between the bottom sulfur atoms and top layer of Au and also top layer of sulfur atoms due to sandwich configuration of MoS_2. The minimum and saddle point of PES's charge density differences and linear charge density can be shown in figure 3.21 .

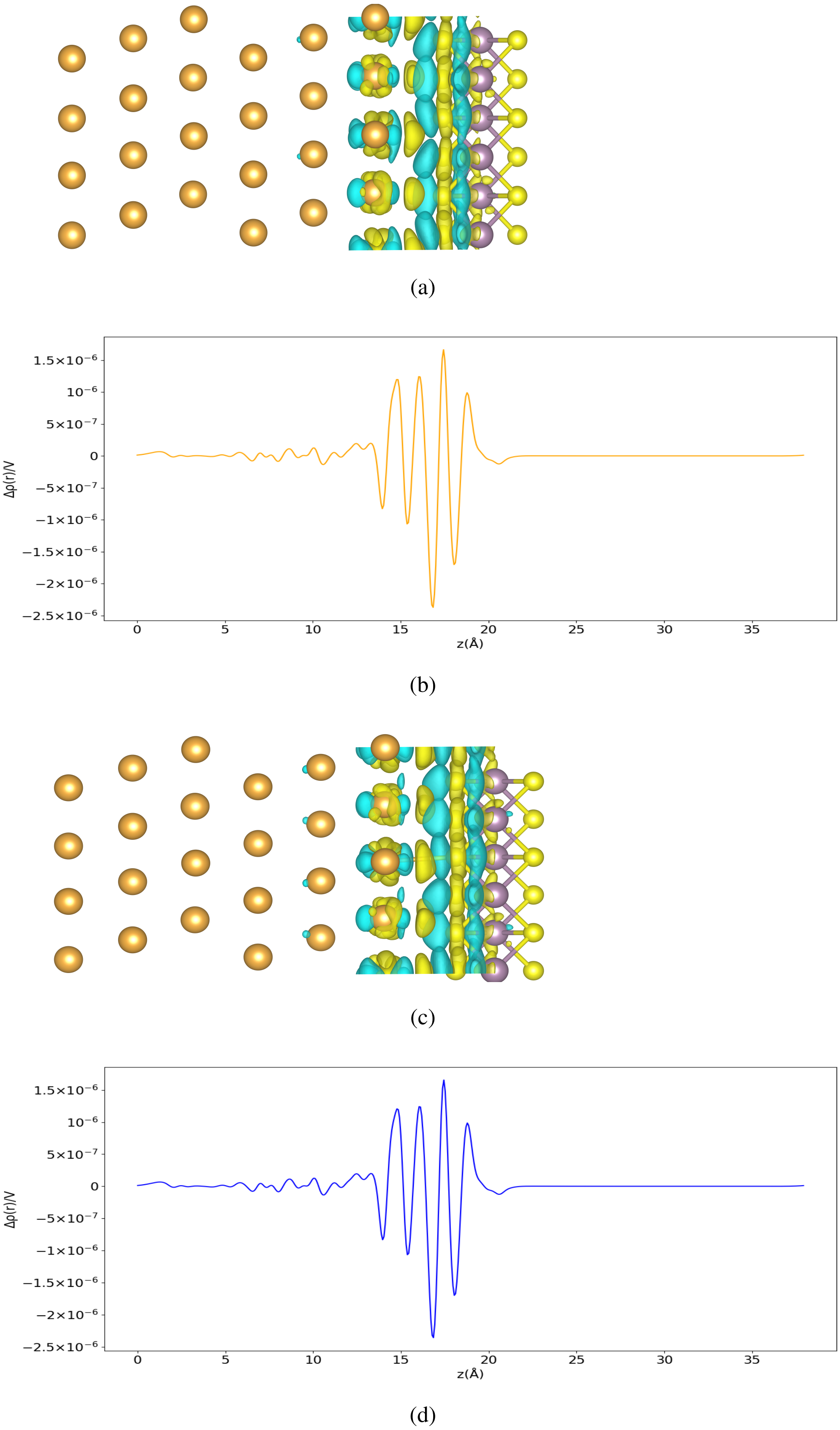

Figure 3.21: Isosurfaces and variation of linear density of charge density difference long z-axis on saddle point (a,b) and on minimum point (c,d) of PES.

CHAPTER 4

CONCLUSION

In this thesis, we have examined the nanotribological properties of the Au(111)/MoS_2 interfaces by modeling them using Density Functional Theory (DFT). Before the examination of friction behavior of the interface, MoS_2's electronic structure, atomic orbital properties and phonon dispersion are studied.

The band structure of MoS_2 is calculated with PBE functional. The optical band gap value has good agreement with previous studies but it was far away from experimental value of optical band gap. Therefore, we decided to increase contribution of exchange-correlation effects inside the KS Hamiltonian with using HSE06 energy functional. This functional with default parameters gave us to much bigger band gap value than PBE functional calculation and also experimental value of band gap due to Hartee-Fock short range energy. So we decided to change Hartee-Fock short range energy quantitative to reach exact experimental value of band of MoS_2. After the arrangement, our result has a good agreement with experimental value of band gap value.

The atomic orbital properties of MoS_2 is studied to understand band gap structure in our previous calculation. For each element of MoS_2, we calculated orbital contribution to band structure. The result give us to good agreement with previous studies.

The phonon dispersion is studied to understand stability of MoS_2 and also vibrational properties of MoS_2 for exploring friction behavior in next studies.

Au bulk structure's lattice constants are contracted by using DFT-D3 functional for consistency with following calculations. After construction the proper Au bulk, we chose to create Au(111) surface for simulating AFM tip. Geometric optimization perform to construct mutual unit cell for Au(111) surface and MoS_2 layer. In this consturction process, we applied strain MoS_2 structure which has not disordered atomic bond between Mo and S elements to fit unit cell of Au(111) surface. The equlibruim distance and minimum interaction energy between MoS_2 and Au(111) are calculated using vdW energy and only KS energy. To reveal source of this energy and distance, charge density difference of the interface is analyzed and the result showed that vdW energy has huge contribution to interaction of the interface. The friction behavior of the interface is investigated in x and y direction for different z distance. The lateral force on top layer of Au(111) surface is calculated by Hellmann-Feynman theorem with using self consistent field iteration for each distance. Each vertical load is constructed by using spline interpolation in the z direction. When magnitude of vertical load increased, lateral forces increase in x direction and a other global minimum point is observed at 0,25 Å after load $2\ eV/$ Å .On the other hand, there are two global minimum point for each load in y direction and after $2\ eV/$ Å harmonic trend broken down, local minimum regions are observed. Average friction forces and friction coefficients under different magnitudes of vertical load have also been investigated and it is found that the average friction force increases with the increase in the vertical load for this system however, friction coefficients decrease almost parabolic trend until $4\ eV/$ Å and $10\ eV/$ Å vertical loads at x,y direction after that friction coefficients has slightly increased trend. The average linear charge densities of $4\ eV/$ Å, $10\ eV/$ Å, $12\ eV/$ Å and $14\ eV/$ Å vertical loads are examined to shed light on increasing trends of friction coefficients. The charge accumulation and depletion on the interface is increased when vertical load is increased. This situation increased coulombic interaction then attractive forces on interface caused increasing of friction coefficient. The potential energy surfaces calculation is performed to obtain most suitable path for sliding MoS_2 layer on Au(111) surface. The energy corrugation is calculated on this path and also critical stiffness of potential wells are calculated and slip-stick regime is observed . To shed light into the mechanism behind friction between surfaces, average charge density of the system was also analyzed by comparing the maximum, minimum and saddle point of potential surfaces. However, not a significant difference was observed in average charge density and transfer between surfaces so we revealed charge dynamics between the interface for maximum point of PES.

In summary, we reveals that the Au(111)/MoS$_2$ interface has lubricant behavior since the friction coefficient of the system is close to the range of the friction coefficients that are used for the definition of the superlubricity even with the presence of a load.

REFERENCES

[1] Hutchings, Ian M (15 August 2016). *"Leonardo da Vinci's studies of friction" (PDF)*. Wear. 360 (Supplement C): 51–66.

[2] Popova, Elena; Popov, Valentin L. (2015-06-01). *"The research works of Coulomb and Amontons and generalized laws of friction"*. Friction. 3 (2): 183–190.

[3] L. Prandtl, *Ein Gedankenmodell zur kinetischen Theorie der festen K¨orper*, Z. Angew. Math. Mech. 8, 85–106 (1928).

[4] Bowden, F.P., Tabor, D. *The Friction and Lubrication of Solids. Clarendon Press, Oxford, 1964.* Part 1, pp.110–121, Part 2, pp. 158–185.

[5] Bowden, F. P., and Tabor, D., 1939, *"The Area of Contact Between Stationary and Between Moving Surfaces"*, Proc. R. Soc. A, 169(938), pp. 391–413.

[6] Paul G. Slade. *Electrical contacts principles and application.*

[7] B. Bhushan. *Nanotribology and Nanomechanics.* Springer, 2008.

[8] W. Nix. *Mechanical properties of thin films. Metall. Trans. A,* 20:2217–2245, 1989.

[9] X. Li and B. Bhusan. *Micro/nanomechanical characterization of ceramic films for microdevices.* Thin Solid Films, 340:210–217, 1999.

[10] M. P. de Boer, H. Huang, J.C. Nelson, Z. P. Jiang, and W.W. Gerberich. *Fracture toughness of silicon and thin film micro-structures by wedge indentation.* Mater. Res. Soc. Symp. Proc., 308:647–652, 1993.

[11] H. Guckel, D. Burns, C. Rutigliano, E. Lovell, and B. Choi. *Diagnostic microstructures for the measurement of intrinsic strain in thin films. J. Micromech. Microeng.* 2:86–95, 1992.

[12] F. Ericson, S. Greek, J. Soderkvist, and J.-A. Schweitz. *sensitivity surface micromachined structures for internal stress and stress gradient evaluation.* J. Micromech. Microeng., 7:30–36, 1997.

[13] L. S. Fan, R. S. Muller, W. Yun, R. T. Howe, and J. Huang. *Spiral microstructures for the measurement of average strain gradients in thin films,* 1990.

[14] M. Biebl and H. von Philipsborn. *Fracture strength of doped and undoped polysilicon,* 1995.

[15] https://commons.wikimedia.org/wiki/File:AFMsetup.jpg

[16] Cahangirov S., Ataca C., Topsakal M., Sahin H., and Ciraci S. *Frictional figures of merit for single layered nanostructures.* Phys. Rev. Lett., 108:126103, (2012).

[17] Cahangirov, S., Topsakal, M., Aktürk, E., Şahin, H., Ciraci, S. (2009). *Two- and One-Dimensional Honeycomb Structures of Silicon and Germanium.* Physical Review Letters, 102(23).

[18] Cahangirov S., Çıracı S., and Özçelik V. O. *Superlubricity through graphene multi-layers between ni(111) surfaces.* Phys. Rev. B, 87:205428, (2013).

[19] Wang L., Zhou X., Ma T., Liu D., Gao L., Li X., Zhang J., Hu Y., Wang H., Dai Y., and Luo J. *Superlubricity of a graphene/mos2 heterostructure: a combined experimental and dft study.* Nanoscale, 9:10846–10853, (2017).

[20] H. Li, J. Wang, S. Gao, Q. Chen, L. Peng, K. Liu, and X. Wei. *Superlubricity between MoS2 monolayers.* Advanced Materials, 29, May 2017. M. Born and J. R. Oppenheimer, Ann. Phys. 84, 457 (1927). https://doi.org/10.1002/andp.19273892002 , Google ScholarCrossref

[21] M. Born and J. R. Oppenheimer, Ann. Phys. 84, 457 (1927) https://doi.org/10.1002/andp.19273892002 , Google ScholarCrossref

[22] D. R. Hartree, Math. Proc. Cambridge 24(1), 89–132(1928).

[23] V. A. Fock, Z. Phys.61(1-2), 126–148 (1930).

[24] W. Kohn and L. J. Sham. *Self-consistent equations including exchange and correlation effects.* Phys. Rev., 140:A1133–A1138, Nov 1965.

[25] Theory of the Inhomogeneous Electron Gas. (1983). doi: 10.1007/978-1-4899-0415-7

[26] Nocedal, J., Wright, S. J. (2006) *Numerical optimization.* New York: Springer.

[27] Perdew, J. P., Burke, K., Ernzerhof, M. (1996). *Generalized Gradient Approximation Made Simple* Physical Review Letters, 77(18), 3865–3868. doi: 10.1103/physrevlett.77.3865

[28] Perdew, J. P., Wang, Y. (1992). *Accurate and simple analytic representation of the electron-gas correlation energy.* Physical Review B, 45(23), 13244–13249. doi: 10.1103/physrevb.45.13244

[29] Lee, C., Yang, W., Parr, R. G. (1988). *Development of the Colle-Salvetti correlation-energy formula into a functional of the electron density.* Physical Review B, 37(2), 785–789. doi: 10.1103/physrevb.37.785

[30] Vosko, S. H., Wilk, L., Nusair, M. (1980). *Accurate spin-dependent electron liquid correlation energies for local spin density calculations: a critical analysis.* Canadian Journal of Physics, 58(8), 1200–1211. doi: 10.1139/p80-159

[31] Heyd, J., Scuseria, G. E., Ernzerhof, M. (2003). *Hybrid functionals based on a screened Coulomb potential.* The Journal of Chemical Physics, 118(18), 8207–8215. doi: 10.1063/1.1564060

[32] Dill, Dan (2006). *Notes on General Chemistry (2nd ed.), Chapter 3.5, Many-electron atoms: Fermi holes and Fermi heaps.*W. H. Freeman. ISBN 0393976610.

[33] Grimme, S., Antony, J., Ehrlich, S., Krieg, H. (2010) *A consistent and accurate ab initio parametrization of density functional dispersion correction (DFT-D) for the 94 elements H-Pu.*he Journal of Chemical Physics, 132(15), 154104. doi: 10.1063/1.3382344

[34] G. Kresse, D.joubert, Phys. Rev. B 59 (1999) 1758

[35] P.E. Blöchl. Phys. Rev B 50(1994) 17953

[36] G. Kresse, J. Furthmüller, Phys. Rev. B 54 (1996) 11169.

[37] Kresse, J. Furthmüller, Comput. Mater. Sci. 6 (1996) 15.

[38] J.A. Wilson, A.D. Yoffe, Adv. Phys. 18 (1969) 193.

[39] D. Yang, S.J. Sandoval, W.M.R. Divigalpitiya, J.C. Irwin, R.F. Frindt, Phys. Rev. B43 (1991) 12053.

[40] Shi, L.-B., Li, M.-B., Xiu, X.-M., Liu, X.-Y., Zhang, K.-C., Liu, Y.-H., … Dong, H.-K. (2017). *First principles calculations of the interface properties of a-Al2O3/MoS2 and effects of biaxial strain.* Journal of Applied Physics, 121(20), 205305. doi: 10.1063/1.4983815

[41] Kośmider, K., and J. Fernández-Rossier. *"Electronic Properties of the MoS2-WS2heterojunction."* Physical Review B 87.7 (2013): n. pag. Crossref. Web.

[42] Scalise, E., Houssa, M., Pourtois, G., Afanasev, V., Stesmans, A. (2014). *First-principles study of strained 2D MoS2.* Physica E: Low-Dimensional Systems and Nanostructures, 56, 416–421. doi: 10.1016/j.physe.2012.07.029

[43] D. Alf´e, Comput. Phys. Commun. 180, 2622 (2009).

[44] Ataca, C., Topsakal, M., Akturk E., Ciraci, S. (2011). *A Comparative Study of Lattice Dynamics of Three- and Two-Dimensional MoS2.* The Journal of Physical Chemistry C, 115(33), 16354–16361. doi: 10.1021/jp205116x

[45] 49C. Kittel, Introduction to Solid State Physics, 7th ed. Wiley, New York, 1996.

[46] Lazić, P. (2015). *CellMatch: Combining two unit cells into a common supercell with minimal strain.* Computer Physics Communications, 197, 324–334. doi: 10.1016/j.cpc.2015.08.038